Orographic Modification of Cyclone Development

ISIDORO ORLANSKI

Geophysical Fluid Dynamics Laboratory/NOAA, Princeton University, Princeton, New Jersey

BRIAN D. GROSS

Geophysical Fluid Dynamics Laboratory/NOAA, Atmospheric and Oceanic Sciences Program, Princeton University, Princeton, New Jersey

(Manuscript received 23 February 1993, in final form 17 August 1993)

ABSTRACT

The orographic modification of cyclone development is examined by means of primitive equation model simulations. When a mature baroclinic wave impinges on an east–west oriented mountain ridge, a relatively intense cyclone forms on the south side of the ridge. This cyclone extends throughout the depth of the troposphere and possesses relatively small vertical tilts, large velocities, and strong temperature perturbations compared to classical baroclinic eddies. The vorticity growth in the orographic cyclone center is larger than that of baroclinic eddies that grow over flat terrain. However, there is no absolute instability associated with this orographic enhancement. A longer ridge produces a more intense eddy.

The behavior of small-amplitude normal modes on a zonally symmetric mountain ridge shows that baroclinic development is enhanced where the topography slopes in the same direction as the isentropes. This is consistent with earlier studies using uniform slopes that show that the heat flux forced by this terrain enhances the conversion of available potential energy. It is shown that the structure of nonlinear waves is similar to that of linear modes over a mountain ridge with steep slopes, in which the cross-ridge flow and the associated heat flux are partially blocked by the mountain.

Simulations of a stationary cold front interacting with a mountain ridge suggest that orographic cyclogenesis is triggered when the mountain ridge locally modifies the frontal circulation as it impinges on the ridge. Warm southerly flow in the front is diverted westward by the mountain ridge, intensifying the strong hydrostatic pressure gradient between the mountain anticyclone and the developing cyclone to the south. In contrast, cold northerly flow is diverted eastward as it approaches the mountain and effectively broadens the mountain anticyclone toward the north. This produces the characteristic pressure dipole observed in orographic cyclogenesis. It is concluded that mature baroclinic eddies approaching the mountain ridge should have a strong frontal zone with a considerable temperature contrast and strong circulation for an intense response.

1. Introduction

Alpine cyclogenesis has attracted a great deal of recent attention, in part due to the availability of the comprehensive dataset that resulted from the Alpine Experiment (ALPEX). Perhaps the most studied example of this so-called "lee cyclogenesis" occurred on 3–6 March 1982 during the ALPEX Special Observing Period. In this case, a deepening upper-level trough approached the European continent and the Alpine massif. A distinct cutoff low formed at 300 hPa directly south of the Alps within 24 hours, as shown in Fig. 1a. During this time, a surface cold front associated with the upper-level trough crossed part of the Alpine massif, and a closed low developed at 1000 hPa (Fig. 1b). High pressure over the Atlantic extends north of the Alps, forming with the closed low to the south a strong pressure dipole across the mountain range that is characteristic of this phenomenon (Mesinger and Pierrehumbert 1986).

The theories that have been proposed to explain this phenomenon approach the problem mainly from two distinct points of view: modifications at the scale of baroclinic waves, and local alterations confined to the environment near the orography. Those theories that concentrate on wave-scale effects ascribe lee cyclogenesis to the interaction between a large-scale baroclinic wave and an isolated mountain range. Pierrehumbert (1985) has shown that an eastward-propagating baroclinic wave that is bisected by a knife-edge mountain produces a symmetric pattern of cyclones and anticyclones both north and south of the barrier, as a consequence of complete low-level flow blocking. Speranza et al. (1985) have proposed a normal-mode theory of lee cyclogenesis wherein the structure of an unstable baroclinic wave is modified by orographic stretching

Corresponding author address: Dr. Isidoro Orlanski, Princeton University, GFDL, Forrestal Campus, Princeton, NJ 08540.

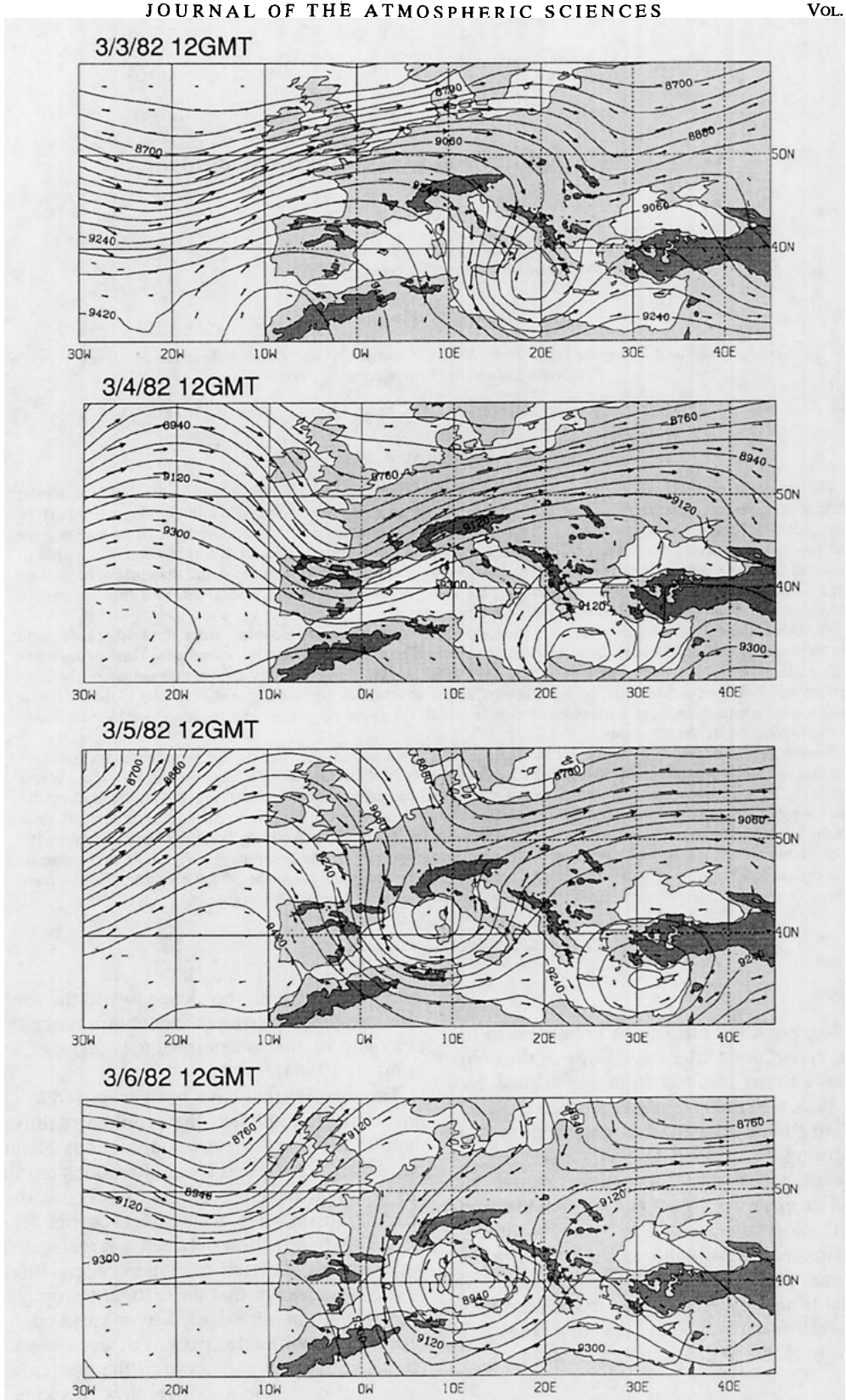

FIG. 1. Development of the 5 March 1982 Alpine lee cyclone in the (a) 300-hPa and (b) 1000-hPa geopotential height and velocity fields for selected times. The contour interval is (a) 60 dam;

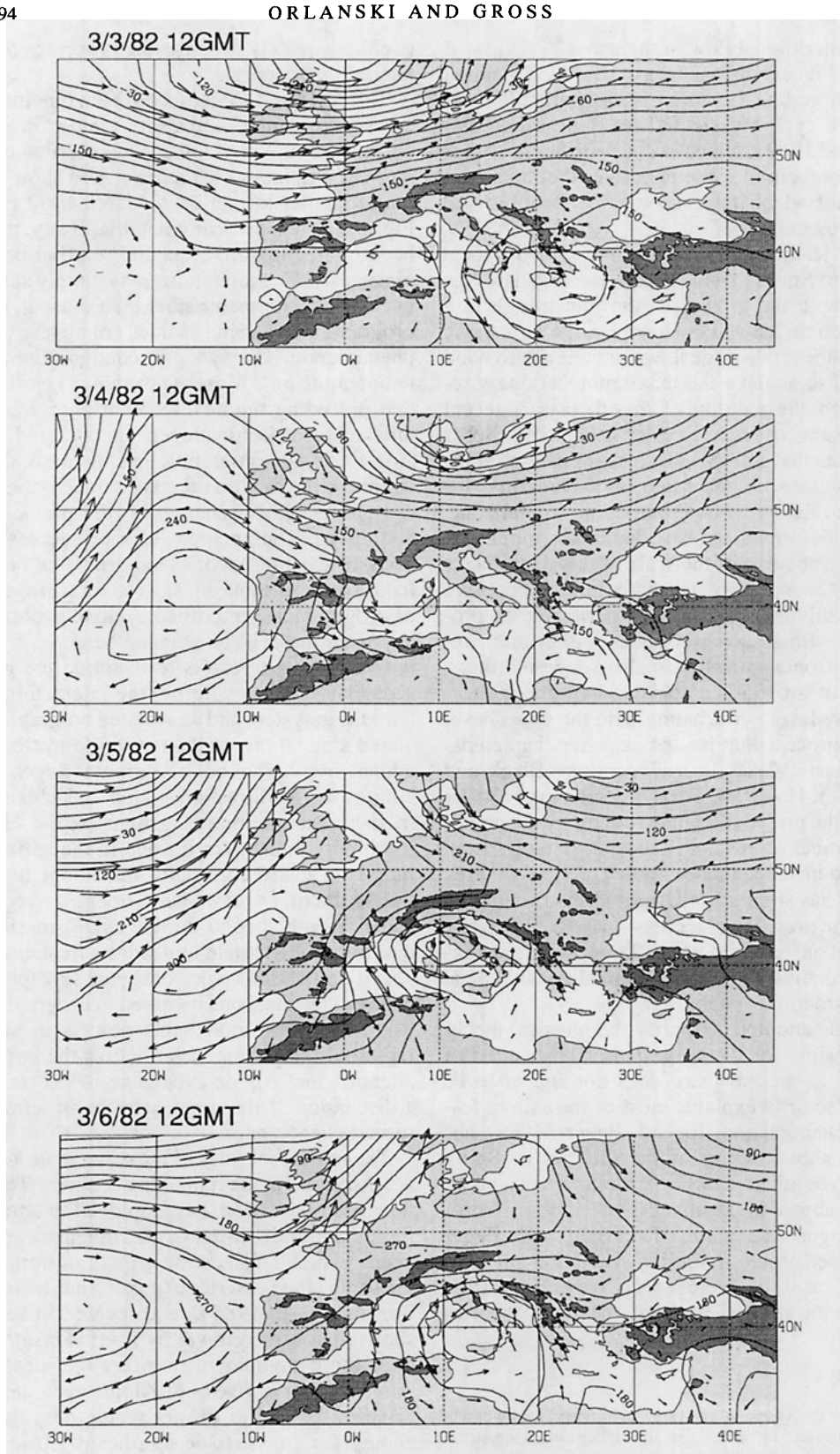

FIG. 1. (*Continued*) (b) 30 dam. The maximum wind speed, corresponding to the longest wind vector shown, is (a) 10 m s^{-1} and (b) 20 m s^{-1}. Land is lightly shaded, and terrain heights greater than 1000 m are darkly shaded.

acting on the meridional flow in the wave. A review of this theory and its extensions is provided by Tibaldi et al. (1990). These linear quasigeostrophic theories describe both lee cyclogenesis and lee anticyclogenesis (Buzzi and Tosi 1989), which occur as different phases of the parent baroclinic wave pass over the mountain, but they cannot adequately account for the observed rapid wave growth.

One of the leading theories dealing with the local effects is that of Smith (1984, 1986). He associates lee cyclogenesis with the growth of the first trough in a standing baroclinic lee wave. However, the unrealistic constraint that the cross-ridge flow contains a zero wind level, required to achieve the maximum stationary response, restricts the validity of this theory. A recent nonlinear quasigeostrophic calculation by Schär (1990) suggests that Smith's mechanism may produce initial perturbations on the scale of a baroclinic lee wave within a relatively broad baroclinic frontal zone, as the latter is deformed and retarded by the mountain. The calculation shows that the scale of this disturbance is limited by the extent of the baroclinic zone. As a consequence, this mechanism may be unable to produce systems with reasonable scales within more realistic narrow frontal zones. It is also suggested that a second phase of growth is associated with the interaction of this low-level perturbation with the upper-level vorticity in a process that possesses some characteristics of Pettersen's Class B cyclogenesis (Bleck and Mattocks 1984). However, Schär's results may also be interpreted as the projection of the forcing by the mountain onto a number of unstable and neutral modes from which the most unstable mode slowly emerges. Finally, his basic state has similar limitations to that in Smith's study in that the presence of a cross-ridge wind reversal in the vertical is required for a large stationary response. This condition is probably unrealistic in typical midlatitude baroclinic zones.

Despite these attempts to clarify the physical mechanisms responsible for the orographic modification of cyclogenesis,[1] at present there does not appear to be one that satisfactorily explains most of the salient features of the phenomenon. Indeed, Egger (1988) has discussed the shortcomings of the theories of Smith (1984), Pierrehumbert (1985), and Speranza et al. (1985) cited above in idealized simulations of orographic cyclogenesis, while Tafferner and Egger (1990) have performed a similar evaluation of these theories with cases of cyclogenesis observed during ALPEX. In both studies, none of the three theories could adequately describe the processes leading to enhanced cyclogenesis.

Tafferner and Egger (1990) have pointed out that a certain amount of ambiguity resides in what exactly constitutes an orographic cyclone. For example, numerical simulations *without the Alps* show cyclone evolution similar to that on 5 March 1982 (illustrated in Fig. 1), so it is unclear what role, if any, the mountains have in creating this "classic" case of orographic cyclogenesis! The mountains may simply serve to *modify* cyclone development rather than cause it. Furthermore, orographic cyclogenesis does not appear to be a robust phenomenon. The synoptic configuration of wind and temperature on 2 March (not shown) closely resembles that preceding the development on 5 March, but significantly weaker cyclogenesis occurred at this time. Any theory of orographic cyclogenesis must also account for the fact that the appearance of an orographic cyclone is rather sensitive to the prevailing synoptic conditions. The apparent lack of success of the large body of existing theories suggests that *both wave and local scales* must be considered for a proper description of orographically modified cyclone evolution. It is this approach that will be pursued here.

Our main purpose is to examine the generation of secondary cyclones during the interaction of a mature baroclinic system and an isolated orographic ridge. Idealized simulations of the entire life cycle of baroclinic eddies impinging on orographic ridges of different lengths are the thrust of section 2. The basic flow used in these simulations is similar to the climatological mean conditions over Europe in the spring. In the solutions, a distinct vorticity maximum is generated to the south of an east–west oriented ridge. Although some resemblance to Alpine cyclogenesis is apparent due to the basic state and ridge orientation, these idealized simulations were designed to capture the basic physical mechanisms involved in orographic cyclogenesis rather than model this process in any particular region of the globe. Nevertheless, the large amount of attention that Alpine cyclogenesis has received invites a discussion of these mechanisms in terms of this observed phenomenon.

The individual roles of the wave scale and local scale are discussed in the remaining sections. The same basic flow used in section 2 is employed to study linear and finite-amplitude *wave-scale* intensification mechanisms, which enhance the growth of normal modes on the south slope of a ridge (e.g., Orlanski and Cox 1973; Speranza et al. 1985), as discussed in section 3. It is shown that wave growth by itself is *insufficient* to produce the development in either the idealized simulations or observed cases of Alpine cyclogenesis, mainly because the eddies do not reside near the ridge long enough for growth to be significant. However, the *local* production of cyclonic vorticity during the interaction of the mature cold front in the baroclinic wave with the mountain occurs rapidly enough and with sufficient

[1] The name "lee cyclogenesis" implies a direction to the incoming flow that is responsible for generating the enhanced cyclogenesis. Since the processes responsible are not exactly elucidated yet, it seems preferable, and the convention will be followed throughout the rest of this paper, to refer to lee cyclogenesis as the orographic modification of cyclogenesis, or orographic cyclogenesis.

strength to account for most of the characteristics of cyclogenesis south of the ridge, as shown in section 4. A summary and conclusions are presented in section 5.

2. Model simulation

a. Model characteristics

Orographic cyclogenesis is examined by means of a primitive equation model on a beta plane (the ZETA model) expressed in the terrain-following coordinate:

$$Z = e^{-\epsilon[(z-h(x,y))/(H-h(x,y))]}, \qquad (1)$$

where z is physical height, $h(x, y)$ represents the orographic profile, and H is the height of the model rigid lid. In the simulations presented here, the Boussinesq approximation is made. Currently, the model is periodic in the zonal direction. However, to isolate the effects of the topography on an incoming baroclinic eddy, damping by sponge layers at both ends of the channel is included. Rigid impermeable walls bound the domain in the meridional direction. A more detailed description of the model equations can be found in the Appendix.

The basic flow is a zonal jet with piecewise linear vertical shear in thermal wind balance with a tropospheric temperature gradient given by

$$\frac{\partial \Theta}{\partial y} = \begin{cases} -\dfrac{f\Theta_0\Lambda}{2g}\left[1 + \cos\left(\dfrac{\pi}{L_y}(y - y_0)\right)\right] \\ \qquad\qquad |y - y_0| \leq L_y, \\ 0 \quad |y - y_0| > L_y \end{cases} \qquad (2)$$

where $f = [10^{-4} + 10^{-11}(y - y_0)]\ \mathrm{s}^{-1}$ is the Coriolis parameter, $\Theta_0 = 302$ K is a reference temperature, and g is the gravitational acceleration. The (piecewise) constant vertical shear Λ is set here to $\Lambda = 0.003\ \mathrm{s}^{-1}$ for $z \leq 8$ km and $\Lambda = 0$ for $z > 8$ km. The width of the jet is $L_y = 5500$ km, and y_0 is the location of the jet axis. This baroclinically unstable flow, shown in Fig. 2, is fixed at the upstream boundary and is perturbed (at the end of the left sponge layer) by specifying the meridional velocity as the time-dependent Eady wave solution with constant amplitude. These perturbations develop into baroclinic waves in the fluid interior that eventually collide with the mountain downstream. The jet axis is placed north of the ridge so that the cold front in a baroclinic wave intersects the ridge in a manner similar to the observations in the spring or autumn over Europe, when most cases of Alpine cyclogenesis occur. It should also be noted that the mountain itself perturbs the basic flow and produces unstable baroclinic waves farther downstream of the ridge.

b. Control solution

The mountain is represented by an isolated ridge 1500 m high with a north–south width of 600 km extending 2600 km in the east–west direction. The meridional profile is Gaussian, while the zonal profile is a plateau with Gaussian slopes. The channel is 25 600 km long, 6600 km wide (257 × 67 points), and 12 km high (13 levels). The model has been integrated past 10 days ($t = T_0$) to allow the small amplitude perturbation at the left boundary to grow into mature eddies that eventually interact with the orographic ridge downstream.

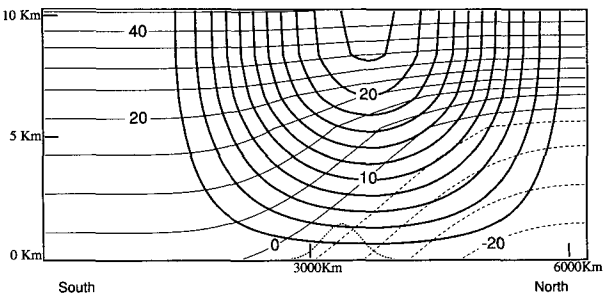

FIG. 2. Potential temperature $\Theta(y, z)$ (thin contours every 5 K) and zonal velocity $U(y, z)$ (thick contours every 2 m s^{-1}) in the basic state used for the control simulations. Negative contours are dashed. Tick marks are placed every 3000 km in the horizontal and every 5 km in the vertical. The mountain profile (dotted line) at the middle of the ridge used in the control experiment is shown for reference.

A distinct relative vorticity maximum appears south of the ridge as the main cyclonic eddy passes to its north, as seen in the upper-level relative vorticity fields in Fig. 3. The isolated vorticity maximum south of the ridge contrasts with the elongated regions of cyclonic vorticity associated with trailing cold fronts in downstream waves. As noted above, these waves develop on the right of the channel from perturbations excited by the imposed orography. They evolve as classical baroclinic eddies over a flat surface and serve as a contrast to those eddies that are directly interacting with the orography on the left of the channel. The orographically modified vorticity extends farther south and is stronger than that associated with the downstream and orographically unperturbed frontal systems.

This southern vorticity center extends throughout the depth of the atmosphere and possesses relatively little vertical tilt compared to the unperturbed downstream baroclinic eddies, as shown in the vorticity cross sections south of the ridge displayed in Fig. 4. Further, the vorticity south of the ridge intensifies rapidly. A comparison of the maximum surface vorticity growth in this eddy with that in the unmodified cyclone (indicated by the arrow in Fig. 3) is shown in Fig. 5. The growth rate of the orographically modified vorticity center (dotted curve) exceeds that of the unmodified wave (dashed curve) throughout the period. However, the vorticity at a fixed point south of the ridge (solid curve) shows only transient growth. The potential temperature signature and meridional and vertical velocities shown in

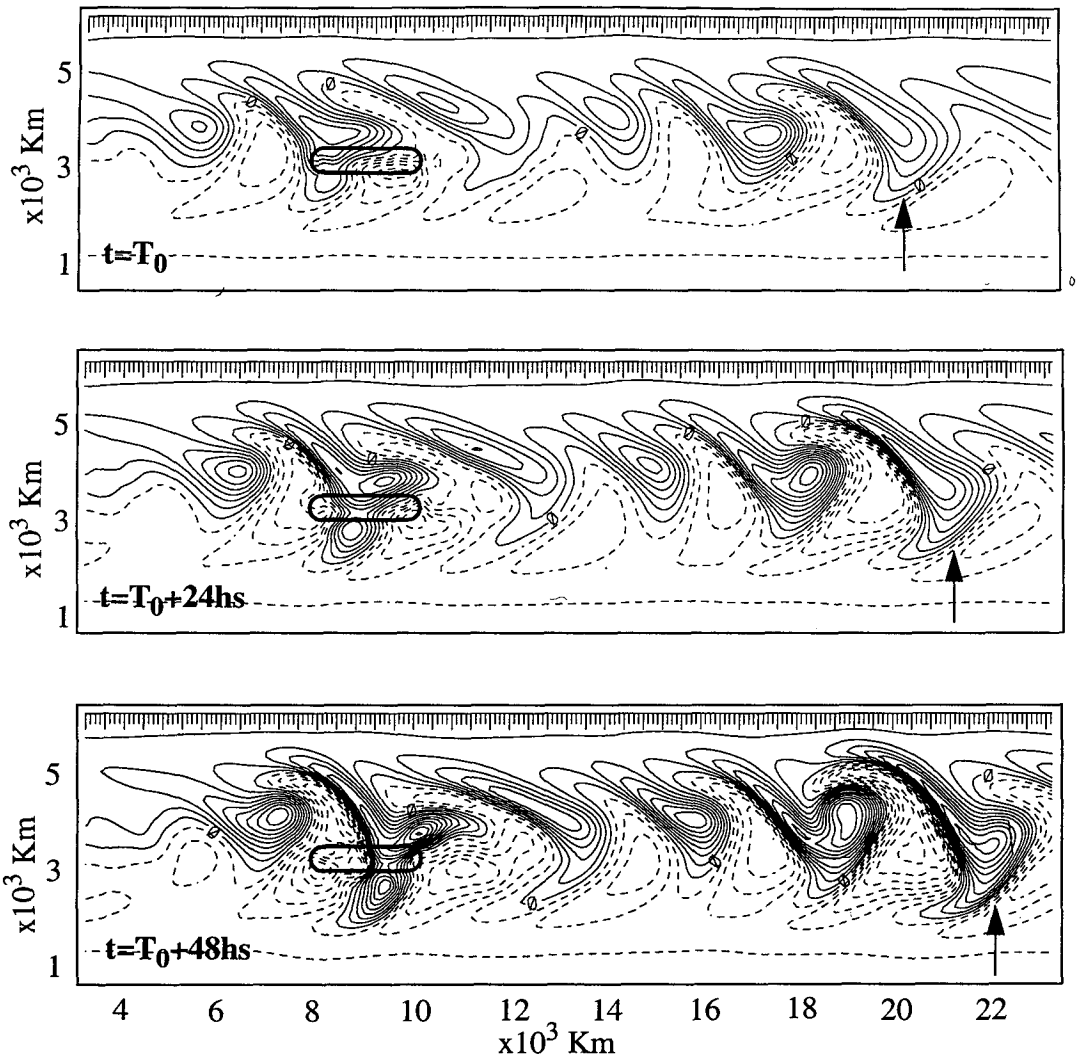

FIG. 3. Development of relative vorticity in the control experiment at $z = 6000$ m and at selected times. The contour interval is 5×10^{-6} s^{-1}, and the heavy ellipse depicts the mountain half-width contour at 750 m. The arrow indicates a baroclinic wave downstream of the ridge that was forced by the orography, as discussed in the text. Tick marks along the upper borders are placed every 100 km.

Fig. 6 reveal strong structural similarities between the unmodified downstream eddies and the orographically modified one. However, the latter exhibits slightly smaller vertical tilts, larger velocities, and stronger potential temperature perturbations.

The potential temperature, pressure, and relative vorticity at the surface ($Z = 1$) when the eddy interacts with the ridge ($t = T_0$) are shown in Fig. 7. The surface pressure minimum on the southern slope is associated hydrostatically with a warm anomaly and the positive relative vorticity in the southern vortex center. These features are displaced southward compared to the undisturbed waves upstream and downstream of the ridge, even though the parent cyclone travels to the north of the ridge. Anticyclonic vorticity, cold air, and high surface pressure directly upstream of the ridge extend eastward into the mountain anticyclone and extend to the north of the ridge to provide, with the cyclone, a pressure dipole across the western end of the mountain. These features are very similar to those observed in the structure of the Alpine cyclone shown at 1200 UTC 5 March 1982 in Fig. 1. We can assume that this solution captures a quite realistic initial development of cyclones modified by the orographic ridge.

The vorticity south of the mountain continues to grow as long as the disturbance flanks the mountain ridge as shown in Fig. 5. However, vorticity growth ceases, and the eddy loses its identity, as soon as it leaves the mountain, as indicated by the surface temperature and wind field displayed in Figs. 8a,b. This

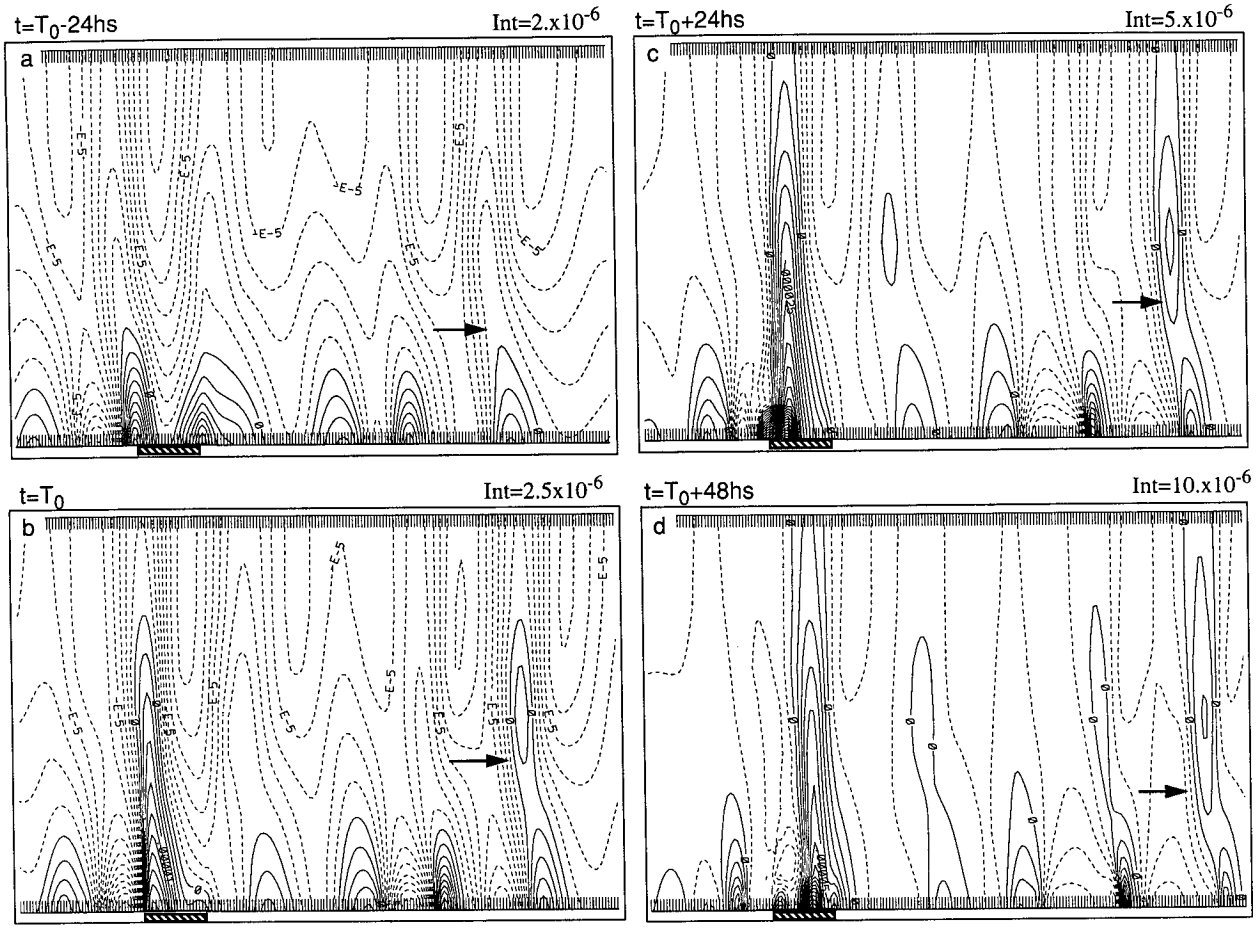

FIG. 4. Cross sections of relative vorticity at (a) $t = T_0 - 24$ h, (b) $t = T_0$, (c) $t = T_0 + 24$ h, and (d) $t = T_0 + 48$ h, through the vorticity center south of the ridge shown in Fig. 3. The contour interval is displayed at the upper right in each panel. Negative contours are dashed. The arrow indicates the same baroclinic wave downstream of the ridge as in Fig. 3. The hatched rectangle at the bottom represents the location of the mountain ridge. Tick marks are placed horizontally every 100 km.

behavior is related to the characteristics of instability in orographic cyclogenesis. The instabilities for the present basic state are of the "convective" type (Merkine 1977); that is, exponential growth is apparent only in a moving reference frame. As shown by the solid curve in Fig. 5, there is no "absolute" instability, that is, exponential growth at a fixed location. This fact calls into question the applicability of normal-mode studies with finite length mountain ridges (Speranza et al. 1985; Trevisan and Giostra 1990; and others). For local features to be possible, either absolute instability is required to produce a rapidly growing response in a local area (local modes) or the disturbances that have grown by convective instability must recross this area repeatedly and undergo successive periods of renewed growth (global modes) (Pierrehumbert 1984, 1986). Our results suggest that, at most, weak absolute instability is present, so that local modes are probably unimportant in orographic cyclogenesis. Global modes are also unlikely to be present because it is highly unlikely that eddies could circumnavigate the earth to recross the Alps, and global modes cannot form at all in the control simulation with sponge layers at the zonal boundaries. Convective instability must predominate, so that the length of the mountain ridge is of paramount importance in determining the further intensification of eddies. This hypothesis can be simply tested by repeating the control simulation with an elongated mountain to verify that the eddies will continue to grow.

c. *Elongated mountain*

To examine the preceding considerations more thoroughly, we have generated a solution with the topography three times longer than in the control solution. The temperature and surface circulation at $t = T_0$ are very similar for both the control (Fig. 8a) and the elongated topography. The comparison of the surface temperature and wind for the control (Fig. 8b) and the elongated topography (Fig. 8c) are shown at the time

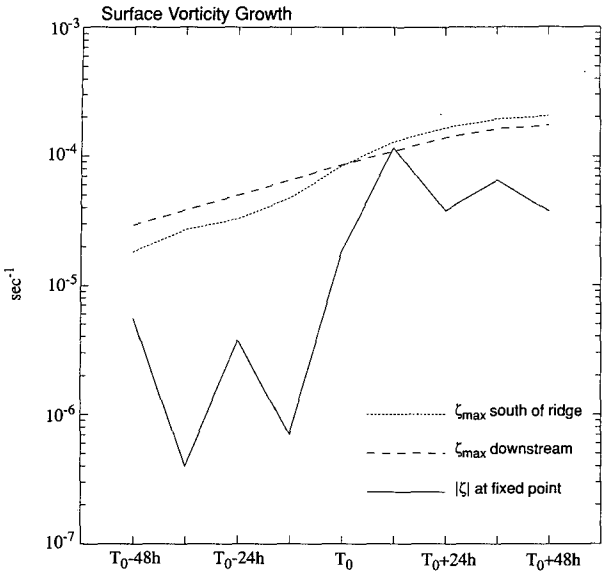

FIG. 5. The growth of the vorticity center south of the ridge (dotted), the downstream vorticity in the baroclinic wave indicated by the arrow in Fig. 4 (dashed), and the absolute value of the vorticity at a fixed point south of the ridge (solid). All measurements were made at the surface.

where the front in the control solution is exiting the region of topography. Note that there is very little wave activity immediately downstream of the extended ridge (Fig. 8c) compared to the shorter ridge (Fig. 8b). Moreover, the elongated ridge has a strong stabilizing influence that significantly suppresses baroclinic growth farther downstream of the ridge. A probable explanation is that the control ridge excites downstream eddies on a scale closer to that of the most unstable baroclinic waves than does the elongated orography.

The fields shown in Fig. 8c reveal that the baroclinic eddies impinging on a ridge produce stronger anomalies to the south as the ridge length, and hence the interaction time with the mountain, is increased. Further, the eddies generated on the north side of the ridge are weaker and possess a considerably shorter wavelength (by a factor of $\sim 2/3$) than the circulations in the south. It seems clear from this comparison that there are strong differences between the evolution of eddies at both local and wave scales on the south and north slopes of the ridge.

The larger wave-scale features are reminiscent of the early normal-mode analyses (Mechoso 1980, among others) of linear baroclinic development over sloping terrain. These studies used zonally symmetric topographies and suggested that positive and negative slopes possess different stability characteristics. However, features of the present case such as the isolated ridge, its position south of the jet, and fully nonlinear development make a comparison with these previous results rather difficult. To remedy this, let us next analyze the impact of these factors on the scale of the baroclinic waves. Since the development in the control and elongated mountain solutions was similar while the eddies flanked the slope, and because the eddies are *convectively unstable* as previously discussed, it is useful to isolate this impact from the local effects at the zonal extremities of the terrain. Thus, we employ *zonally symmetric* mountains in the following analysis.

3. Wave-scale effects

The influence of topographic slopes on the growth rates of linear baroclinic waves has been investigated by Orlanski (1969), Blumsack and Gierasch (1972), and Mechoso (1980), among others, and Orlanski and Cox (1973) have addressed the nonlinear regime in the context of the initial value problem. The main conclu-

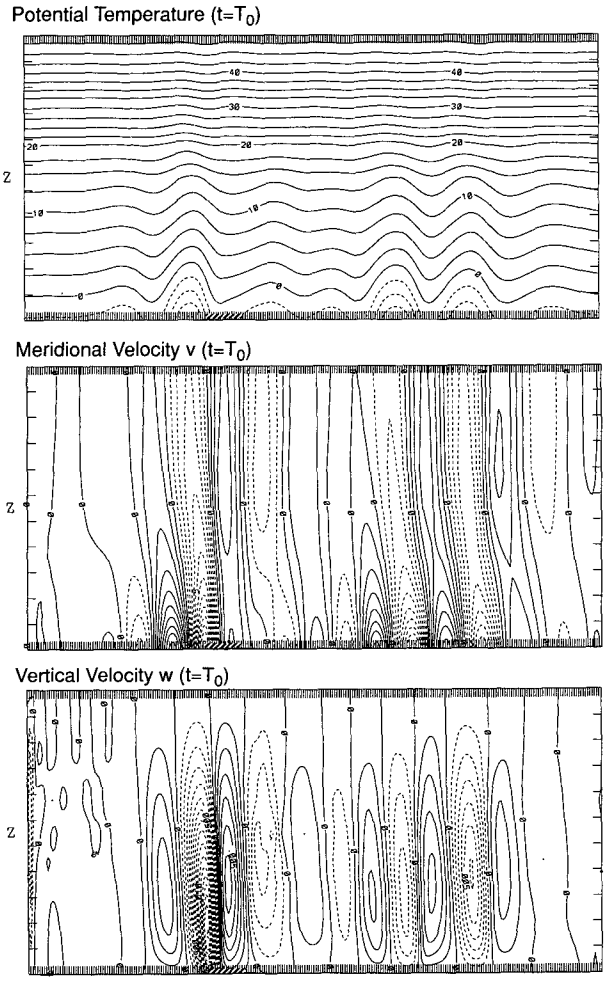

FIG. 6. Cross sections of potential temperature (top, contours every 2.5 K), meridional velocity (middle, contours every 1 m s^{-1}), and vertical velocity (bottom, contours every 0.001 m s^{-1}) through the vorticity center south of the ridge at $t = T_0$ shown in the middle panel of Fig. 3. Negative contours are dashed. Tick marks are placed every 100 km in the horizontal and every 1 km in the vertical.

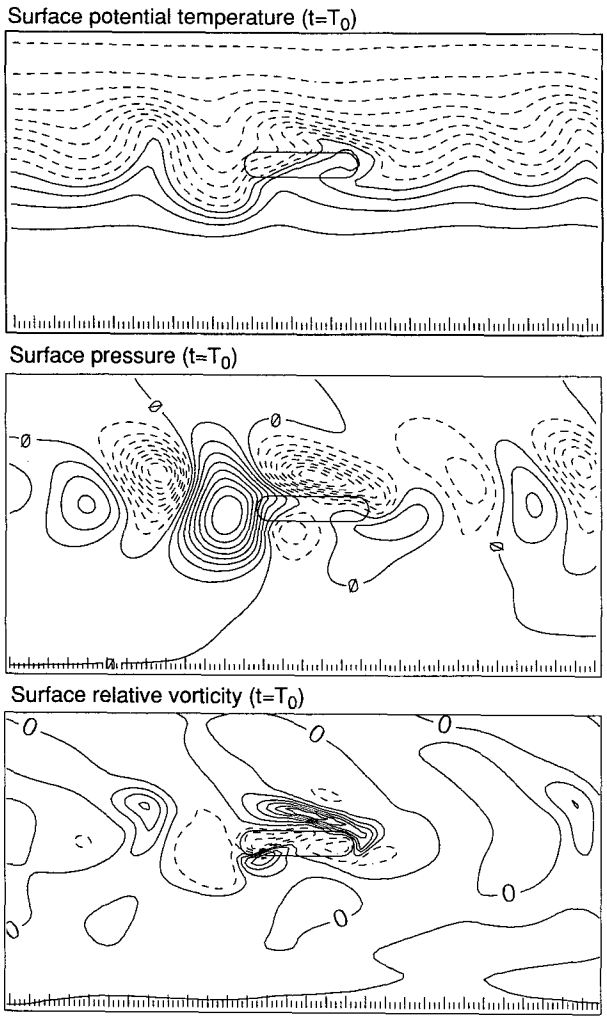

FIG. 7. The surface potential temperature (top, contours every 1 K), pressure anomaly (middle, contours every 1 hPa), and relative vorticity (bottom, contours every 2×10^{-5} s^{-1}) at $t = T_0$ of the control simulation. Negative contours are dashed. The ellipse indicates the mountain half-width. Tick marks along the bottom borders are placed every 100 km.

sion of the linear studies is that the stability depends on the relation of the topographic slope to the slope of the isentropes. Instability is enhanced when the relative slopes force the flow near the surface to move within the "wedge of instability" (Pedlosky 1987, section 7.6) and release available potential energy. One consequence is that under typical Northern Hemisphere conditions, development is concentrated on the south slope of a zonally symmetric ridge, as shown in linear quasigeostrophic (Speranza et al. 1985; Buzzi and Speranza 1986) and nongeostrophic (Malguzzi et al. 1987) normal-mode calculations.

The evolution of the eddies in the elongated ridge solution exhibits some of the features suggested by these linear theories, such as the enhanced development on the south slope of the ridge and a tendency for weaker eddies and shorter wavelengths on the north side (Fig. 8c). However, since the basic state jet (2) is placed north of the ridge, consistent with the springtime climatological position of the jet over Europe, it is important to confirm that the fundamental aspects of the linear solutions are present in the normal modes for this configuration. These results will be used to interpret the extension of these calculations to finite amplitude, which more accurately reflects the growth in the simulations presented in section 2.

a. Zonal symmetric ridge: Linear response

Linear normal modes were calculated by integrating the nonlinear primitive equation model for short periods and renormalizing the zonal perturbation after each period. This procedure should closely approximate the development of eigenmodes in the formally linearized model. The mean flow is that of the control simulation (Fig. 2), but the sponge layers have been removed at the left and right boundaries. The mountain ridge has a Gaussian profile and the same meridional location as that of the previous solutions. The resolution is increased so that the channel is 8480 km long by 6370 km wide (161 × 99 points) and 12 km high (23 levels). Four solutions with different mountain heights h_{max} and e-folding widths L_h will be discussed: (a) $h_{max} = 0$ (no topography); (b) $h_{max} = 500$ m and (c) $h_{max} = 1500$ m, both with $L_h = 300$ km; and (d) a narrow mountain with $h_{max} = 1500$ m and $L_h = 100$ km. The low mountain (b) is comparable to that used in the large body of the normal-mode quasigeostrophic studies (e.g. Speranza et al. 1985), and the higher mountain (c) is similar to that used in the nongeostrophic analysis of Malguzzi et al. (1987). The steep, narrow mountain (d) is closer to that used by Pierrehumbert (1985), in which the ridge is represented by an impermeable barrier of zero thickness in the lower layer of a two-layer model. It should be noted that although the perturbations remain small in the current model integrations, the mountain in all cases has a finite height.

Extended integrations of these cases have been performed to ensure the appearance of the most unstable mode. These calculations show several features that are consistent with analyses of baroclinic instability over sloping terrain. The surface pressure anomalies for the four linear solutions are displayed in Fig. 9. The largest growth rates (approximately 0.91 day^{-1}) occur without any terrain (Fig. 9a). This solution is the classical baroclinic normal mode for the wind profile under investigation. The low mountain (Fig. 9b) with shallow slopes merely distorts the form of the normal mode; it does not qualitatively change the characteristics of the mode. The amplitudes are weaker because of the smaller growth rate (about 0.54 day^{-1}), with low pressure amplitudes slightly stronger than high pressure amplitudes, but the maxima remain north of the mountain

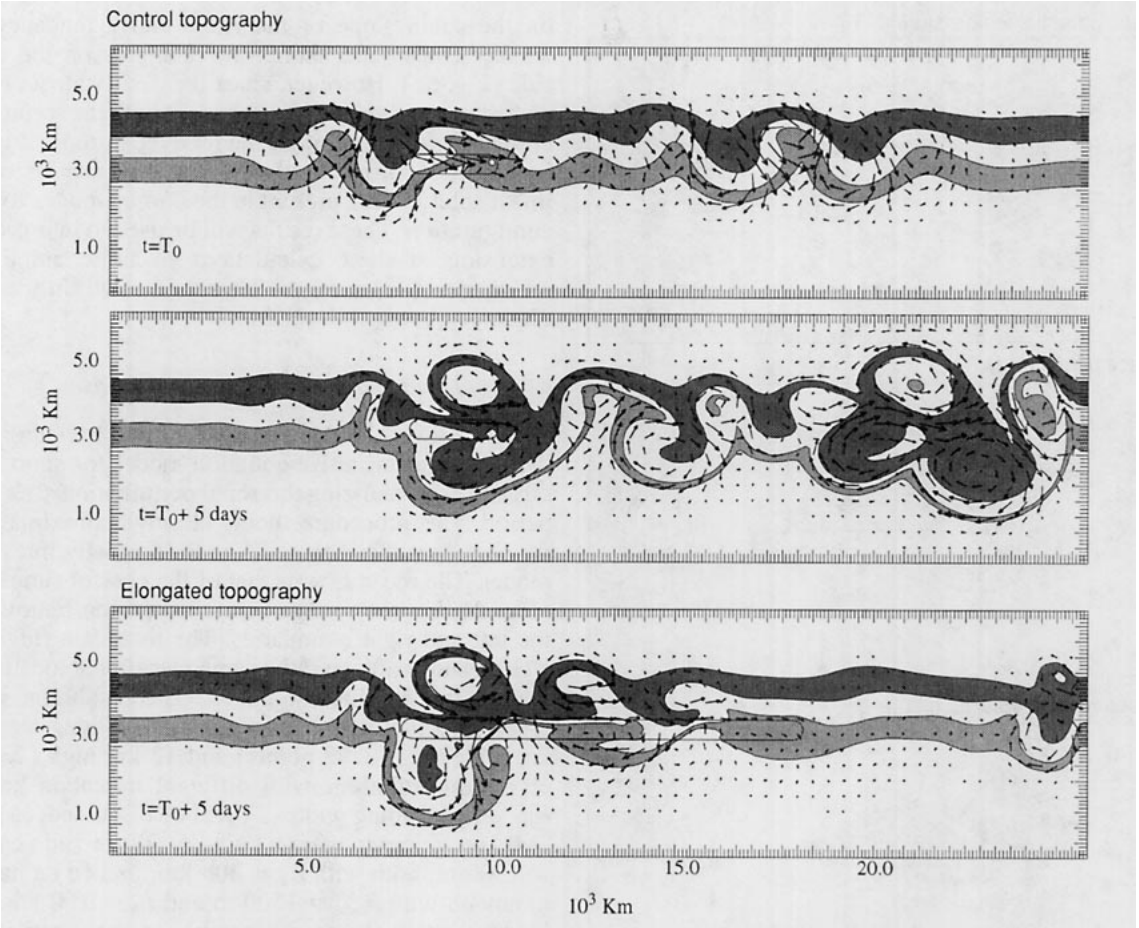

FIG. 8. Potential temperature and horizontal velocity at the surface for the control simulation at $t = T_0$ (top) and $t = T_0 + 5$ days (middle), and for the simulation with elongated topography at $t = T_0 + 5$ days (bottom). The temperature bands correspond to $\theta < 2$ K (white), 2 K $\leq \theta < 2.5$ K (dark), 2.5 K $\leq \theta < 3$ K (white), 3 K $\leq \theta < 4$ K (light), and θ 4 K (white), with cooler temperatures to the north. The longest vector corresponds to a speed of 16 m s^{-1} in (a), 40 m s^{-1} in (b), and 30 m s^{-1} in (c). Tick marks are placed every 100 km.

along the jet axis. As the mountain height increases (Fig. 9c), the low-level structure of the mode changes drastically and the growth rate increases. Enhanced development and maximum perturbation amplitudes occur along the southward-facing slope while development is suppressed along the northward-facing slope (Fig. 9c). This solution is similar to the one presented by Malguzzi et al. (1987). However, as the mountain width narrows (Fig. 9d), communication between the south and north slopes decreases as the cross-ridge flow becomes increasingly blocked. The growth rate increases slightly, and the amplitudes of the disturbance on the north and south slopes are commensurate. Although this aspect of the solution is similar to that of Pierrehumbert (1985), the pressure shown in Fig. 9d has a strong dipolar structure, whereas the two-layer solution of Pierrehumbert possesses a symmetric pressure distribution.

The behavior of these solutions can be easily interpreted by heat flux considerations, although equivalent conclusions can be drawn from potential vorticity arguments (Trevisan and Giostra 1990). Vertical heat fluxes are generated at the lower boundary that enhance the conversion from available potential energy to the kinetic energy of the unstable modes. Basically, on the south slope warm southerly flow is forced to ascend and cold northerly flow is forced to descend, thereby enhancing the release of available potential energy. On the north slope, however, this baroclinic conversion is inhibited as cold air is forced to rise and warm air to sink. It should also be pointed out that the most unstable normal mode has a meridional scale commensurate with the zonal wavelength, and if the meridional heat fluxes are blocked by the topography, the resultant normal mode will have a narrower meridional scale and smaller growth rate consistent with the results of classical baroclinic instability theory. In fact, the narrow mountain case (Fig. 9d) will have a mode with a meridional structure and growth rate more compatible with that of a channel with half the original width. Fur-

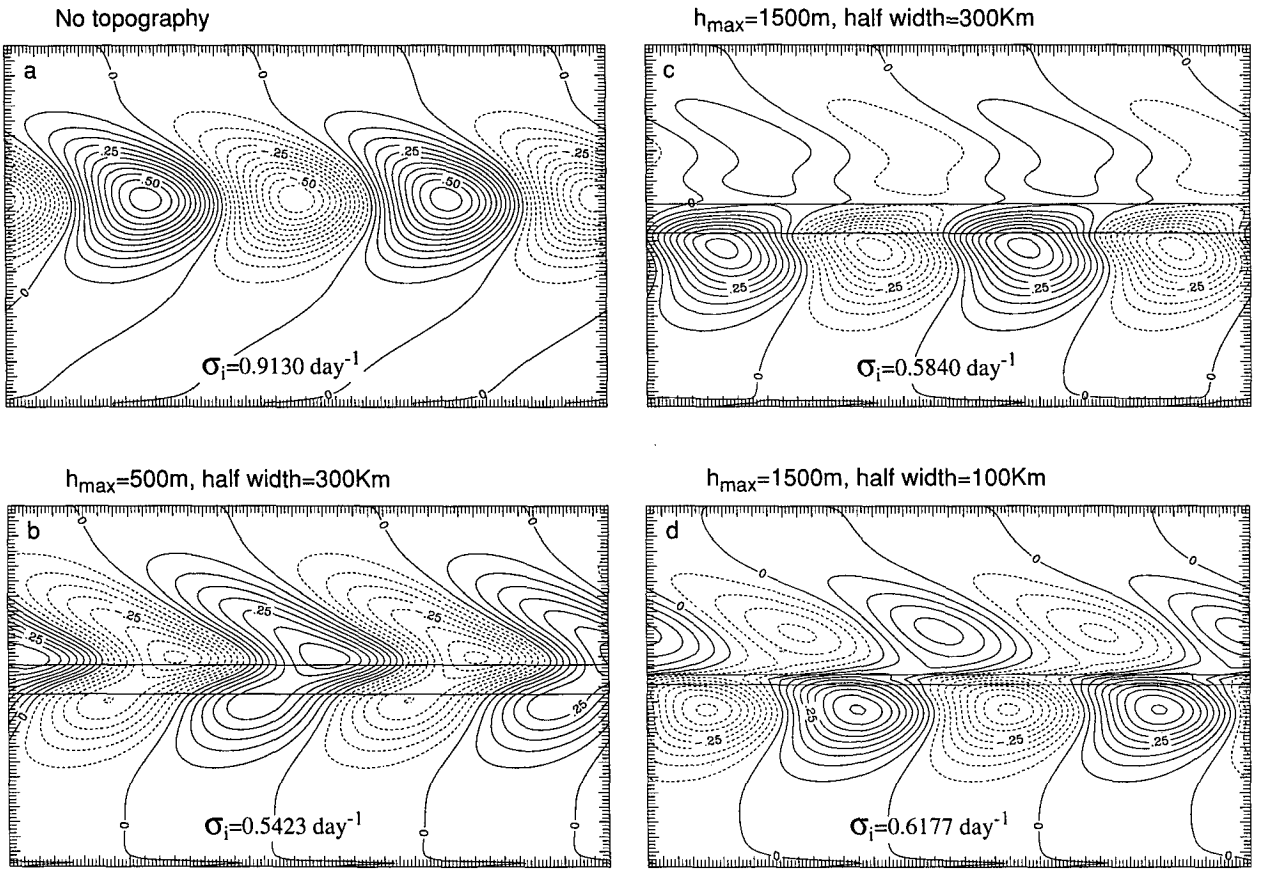

FIG. 9. Normalized surface pressure anomalies in the linear simulations of flow with a zonal mountain. The horizontal lines indicate the mountain half-width. The contour interval is 0.05, and negative contours are dashed. (a) No topography, (b) a low wide mountain, (c) a high wide mountain, and (d) a high narrow mountain. The mountain parameters are shown above each panel. Tick marks are placed approximately every 60 km.

thermore, when the flow is completely blocked at lower levels, as in the two-layer calculations by Pierrehumbert, a symmetric pressure distribution and the associated geostrophic flow discontinuity is allowed across the ridge. However, when the blocking is incomplete, the large shears generated in these symmetric modes would be quickly removed by instabilities. Continuity in the flow along the ridge peak requires the antisymmetric pressure distribution shown in Fig. 9d.

These results confirm that baroclinic instability may be enhanced on the southern slope of a ridge compared to the northern slope when the ridge is south of the jet axis. However, the growth rates associated with this linear process are 0.5–0.6 day^{-1} and are rather small to adequately account for the development in the numerical simulation of over 0.9 day^{-1} (derived from Fig. 5). It is apparent from the control as well as from the elongated mountain case that nonlinear effects of the flow in close proximity to the ridge, especially those associated with heat and vorticity fluxes, are significant. These effects can be captured in fully nonlinear solutions with the zonally symmetric ridge.

b. Zonally symmetric ridge: Finite-amplitude response

Nonlinear effects may be assessed with integrations of the full nonlinear model with the zonally symmetric ridge used above (Fig. 9c). The results are summarized in Fig. 10. The surface wind vectors show strong cyclonic/anticyclonic circulation on the south of the ridge (see Fig. 10a) as suggested by the linear calculations, and they are similar to the patterns shown for the elongated mountain (Fig. 8c). The surface pressure pattern shown in Fig. 10b also possesses features recognizable in the linear calculations. In particular, the intensification of the modes on the south slope of the ridge, shown in Fig. 9c, and the separation of the modes on the north and south slopes due to the blocking of the narrow mountain, shown in Fig. 9d, are both present in this nonlinear solution (Fig. 10b). Since the nonlinear solution has the same mountain profile as the corresponding linear solution shown in Fig. 9c, the comparison shows that nonlinearity enhances the mountain blocking effect

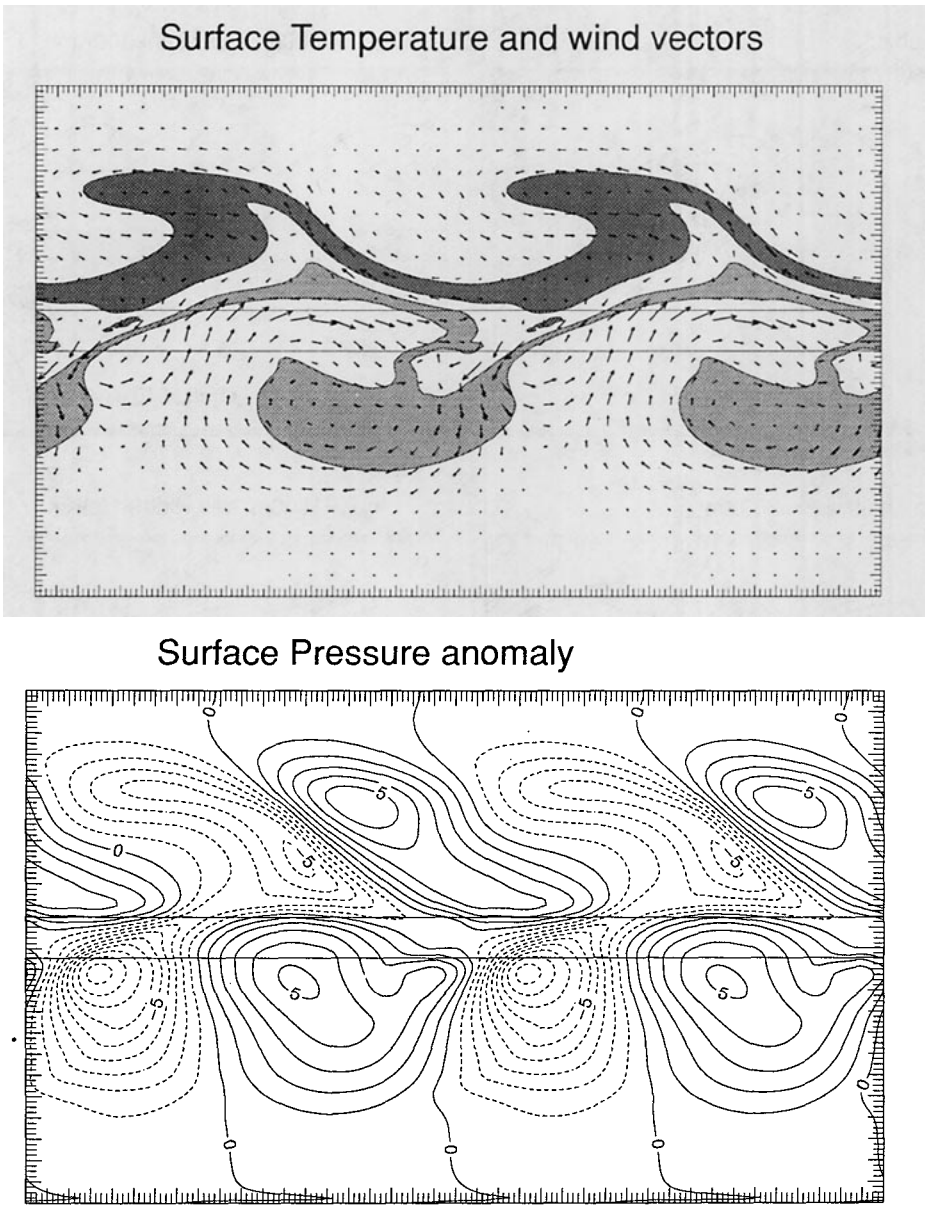

FIG. 10. (Top) Surface potential temperature and velocity in the nonlinear simulation of flow with a zonal mountain. The temperature bands are shaded as in Fig. 8, and the longest wind vector corresponds to a speed of 25 m s^{-1}. The horizontal lines indicate the mountain half-width. Tick marks are placed approximately every 60 km. (Bottom) Surface pressure anomaly in the same experiment. The contour interval is 1 hPa, and negative contours are dashed.

in a manner similar to the linear simulations shown for the narrow mountain case. This nonlinear solution also has strong similarities to those of oceanic baroclinic eddies over the Florida Current (Orlanski and Cox 1973) where the topography across the Gulf Stream is abrupt. In both cases, the nonlinear solution has all the characteristics of baroclinic eddies but with a narrower meridional structure than the most unstable modes without topography.

c. *Discussion of the wave-scale effects*

It has been shown that linear modes are more unstable for the given basic flow in a channel without topography because a finite height ridge reduces the overall extent of the meridional heat fluxes. This can explain why some simulations of Alpine cyclogenesis have shown a larger response without the orography (Tafferner and Egger 1990). Also, an orographic ridge with a

moderate positive slope (in same direction as the isentrope surfaces) can support baroclinic development, whereas on the negative slope this development is strongly inhibited, consistent with studies using uniform slopes (i.e., Mechoso 1980). It has been shown that if the slope is steep enough, it behaves like a wall and the ridge can effectively split the unstable modes in two (Pierrehumbert 1985). The nonlinear normal-mode solution displays features of frontal evolution that are similar to those seen in the initial value problem; for example, the surface pressure dipole across the ridge is well represented in both solutions. Despite these structural similarities, growth rates seem to be small, about half that seen in the control solution. It seems that the nonlinear solution feels the blocking effect, and the consequent inhibition of growth, for even moderate slopes.

Clearly, the south slope of the topography can have a positive contribution to baroclinic development as shown in the solutions with zonally symmetric mountains. However, with a finite length ridge, the eddies must feel the influence of the topography on a time scale that is sufficient for the unstable mode to emerge; say at least of the order of the inverse of the growth rate σ_i. However, the time scale is given for these advected eddies by the length of the mountain ridge L_m divided by the advecting speed $U(z_0)$, the velocity at the steering level z_0. Therefore, the unstable mode will emerge on the south slope of the mountain if the flow satisfies

$$\frac{\sigma_i L_m}{U(z_0)} > 1. \tag{3}$$

An estimate of the growth rate may be provided by the Eady wave growth rate given by

$$\sigma_i = \frac{0.3 f_0 \Lambda}{N}, \tag{4}$$

where Λ and N are the vertical shear and the Brunt–Väisälä frequency estimated in the lower layers of the atmosphere. An estimate of the steering velocity is given by

$$U(z_0) = U_0 + \Lambda z_0. \tag{5}$$

If these expressions are used in (3), this may be rewritten as

$$\frac{(0.3 f_0/N)\Lambda L_m}{(U_0 + \Lambda z_0)} > 1. \tag{6}$$

For $U_0 = 0$ as in the control simulation, and recognizing that the Rossby radius of deformation $L_R = Nz_0/f_0$ is the order of 1000 km and $L_m = 2000$ km, (6) becomes $0.3\, L_m/L_R \sim 1$. Only in cases where surface easterly winds ($U_0 < 0$) are predominant with westerly shears will condition (6) be met, and the waves will have sufficient time for the linear growth to be significant. This condition coincides with that required for absolute instability for most baroclinic flows (Pierrehumbert 1986). However, the required length from (6) to evoke a significant response under mean westerly conditions was not met in the observed Alpine cases discussed in the Introduction, nor in the numerical simulations presented in section 2, where it was established that the orographic disturbance was convectively unstable. As a consequence, the *rapid development of the vorticity center on the south slope* cannot be adequately explained by the *wave-scale enhancement of baroclinic instability*. Moreover, the observations show that horizontal scales of the baroclinic disturbance are larger than the Alpine ridge, which is contrary to the requirement for establishing the linear normal modes. Therefore, additional mechanisms must be operating to produce the development shown above. In the next section we will show that finite-amplitude local effects play a major role in further intensifying an already developing baroclinic eddy.

4. Finite-amplitude response: Local effects

The advection of the potential temperature field in the baroclinic waves by the mountain anticyclone is clearly an important mechanism in the preceding nonlinear simulations. For example, a well-developed frontal system is impinging on the mountain ridge from the west in Fig. 7a. The surface temperature distribution in the control simulation shows a pool of cold air behind the front being advected toward the topographic ridge and distorted by the mountain anticyclone. Further, the arrival at the ridge of the front and its associated surface vorticity (Fig. 4a) seems to precede the strong orographic cyclogenesis described in Figs. 4b–d. Since a front is a manifestation of finite-amplitude cyclogenesis, the modification of its circulation by orography is clearly absent in any linear theory. Let us then consider the characteristics of the frontal circulation during the development of the orographic cyclone. The cross-stream circulation associated with the front at the time of the intersection with the ridge in the control solution has been displayed in Fig. 6. Strong southward flow associated with a cold air anomaly is approaching the topographic ridge at $t = T_0$. The local modification of this circulation by the orography will be shown to be important in the subsequent development of the orographic cyclone and is examined here with high-resolution simulations of an idealized finite-amplitude frontal zone interacting with the ridge. These simulations facilitate the separation of local processes from wave-scale effects during cyclogenesis.

A simple basic state is constructed to represent the frontal system that intersects the ridge in the control experiment. For example, the front at the western end of the ridge in Fig. 6 (control experiment at $t = T_0$) is shown at $t = T_0 + 24$ h in Fig. 11. In these local experiments, the initially two-dimensional frontal circulation is just superposed over an elongated mountain ridge oriented perpendicular to the front. Due to model

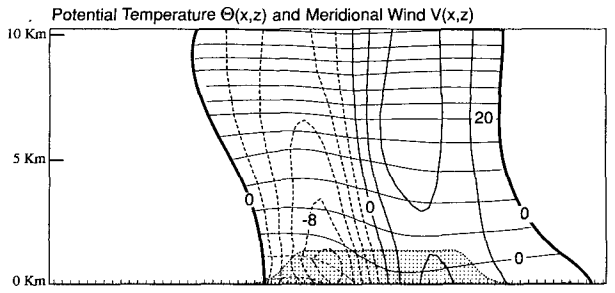

FIG. 11. Potential temperature $\Theta(x, z)$ (thin contours every 4 K) and meridional velocity $V(x, z)$ (medium contours every 2 m s^{-1}) in the front south of the mountain ridge at $t = T_0 + 24$ h in the control solution. Negative velocity contours are dashed and indicate flow out of the page (northerlies). Tick marks are placed every 100 km in the horizontal and every 5 km in the vertical. The stippled region represents the profile of the mountain ridge.

constraints, this simulated frontal circulation is stationary relative to the mountain ridge, but as will be seen, the rapid development of the response makes the comparison to the control experiment unambiguous. The basic state captures the important characteristics of fronts in mature eddies as seen in the control simulation (Fig. 11), namely, the horizontal shear and temperature gradient. Each of these features will be considered in turn to distinguish their individual contributions to cyclogenesis. The channel in these simulations is 5760 km long by 5880 km wide (97 × 99 points) and 12 km high (33 levels). For ease of interpretation the figures and the accompanying discussion will refer to a rotated system in which the channel extends in the north–south direction along the front.

a. Barotropic initial state

For simplicity we first consider the effects of horizontal shear on the development of the southern vorticity center shown in Fig. 4. These effects may be isolated by considering a stably stratified barotropic flow with adjacent bands of positive and negative relative vorticity (no surface temperature variation) given by

$$V(x) = -10 \frac{\sinh\left[\dfrac{(x - x_f)}{L_f}\right]}{\cosh^2\left[\dfrac{(x - x_f)}{L_f}\right]}, \qquad (7)$$

where x_f is the position of the front, which has a horizontal scale of $L_f = 450$ km. A cross section of this basic flow is shown in Fig. 12. The mountain height and width are the same as in the control solution. The interaction of this shear zone with the mountain circulation essentially produces a superposition of the cyclonic/anticyclonic frontal flow and the mountain-induced anticyclone. Within this circulation, illustrated in Fig. 13, flow with cyclonic vorticity will be advected westward south of the ridge and eastward north of the ridge by the mountain anticyclone. All fields are symmetric about the ridge line. The solution shown evolves slowly enough to be considered in a steady state. Nonlinear steady-state barotropic solutions (Pedlosky 1987, section 3.13) achieved by prescribing different inflow and outflow boundaries were also investigated (not shown here). Those steady-state solutions possessed most of the features shown in Fig. 13; however, none of them possessed the clear eastward and westward displacement of the cyclonic centers featured in Fig. 13. It is suspected that either the solution shown in Fig. 13 has not yet reached a true steady state or, since the steady-state calculation assumes potential vorticity conservation along the streamlines, the integration becomes inaccurate in areas of mixed inflow and outflow boundaries because the correct boundary conditions at outflow points cannot be specified a priori. In fact, the largest deviations are observed where the boundary velocity is zero. Special care must be given to integration in those regions.

The circulation shows that the modification of the cyclonic vorticity at each side of the ridge is suggestive of the vorticity pattern in the control solution, but it also seems apparent that some important features are absent. For instance, the circulation in Fig. 13 indicates that the vorticity deformed by the induced mountain flow will not increase further. The vorticity is simply advected by the mountain anticyclone, and since no other sources of cyclonic vorticity are present, the maximum vorticity will be the same as the positive vorticity of the incoming flow. Moreover, the symmetry shown in this barotropic case seems to be inconsistent with the important fact that the orographic cyclone developed on only one side of the ridge. It also seems clear that a more realistic portrait of the frontal flow that impinges on the topography in the control solution can be achieved by including sur-

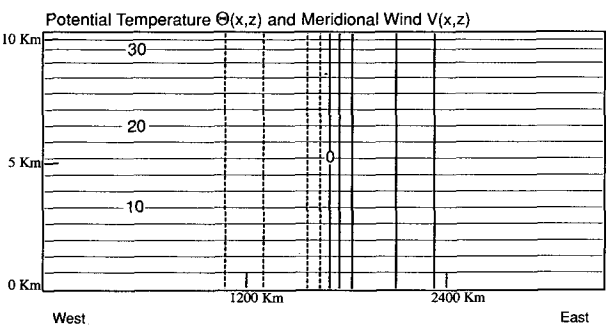

FIG. 12. Potential temperature $\Theta(x, z)$ (thin contours every 2 K) and meridional velocity $V(x, z)$ (thick contours every 2 m s^{-1}) in the basic state used in the simulation of a barotropic front over a mountain ridge. Negative contours are dashed and indicate flow out of the page (northerlies). Tick marks are placed every 1200 km in the horizontal and every 5 km in the vertical.

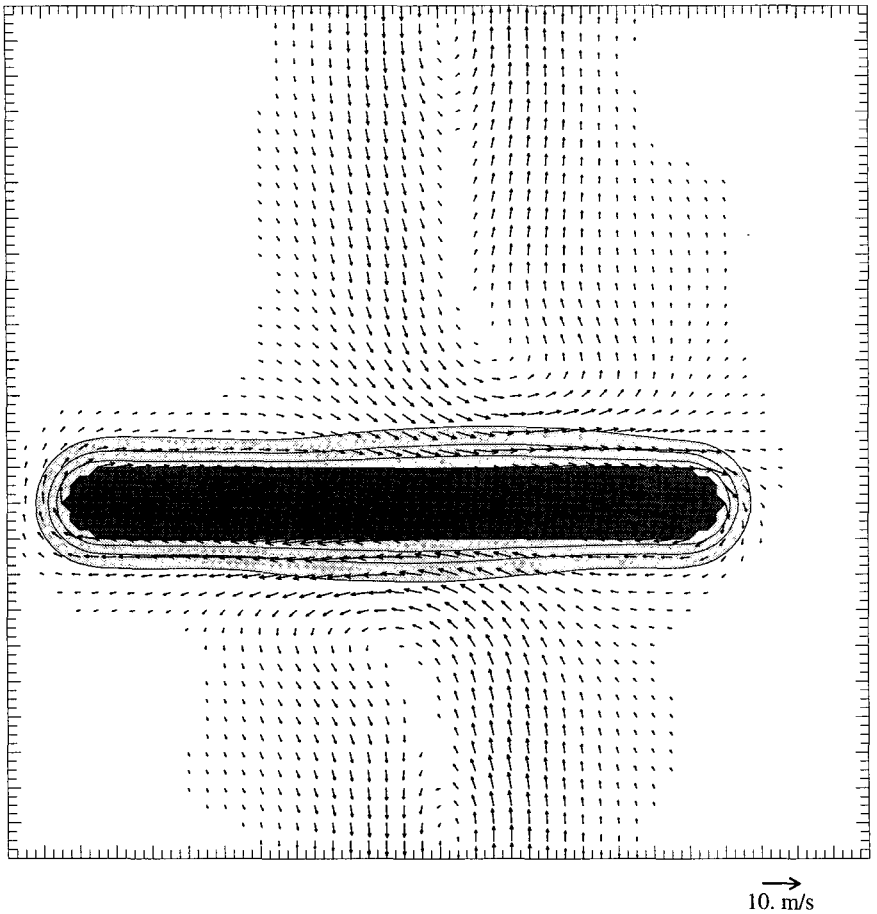

FIG. 13. Potential temperature and horizontal velocity at $z = 1000$ m for the barotropic simulations. The temperature bands correspond to $\theta < 3$ K (light gray, contour interval of 1 K) and $\theta \geq 3$ K (white). The topographic cross section at this height is shaded black. The longest vector corresponds to a speed of 10 m s^{-1}. Tick marks are placed every 60 km.

face heat advection. This baroclinic effect can be simply accomplished by adding to the previous basic state a shallow baroclinic vorticity component with its associated horizontal surface temperature gradient (similar to that shown in Fig. 11).

b. *Baroclinic initial state*

A geostrophic flow in thermal wind balance with a weak horizontal temperature gradient has been included in the barotropic circulation given by (7). The new basic flow is described by

$$V(x,z) = -10\gamma \frac{\sinh\left[\dfrac{(x-x_f)}{L_f}\right]}{\cosh^2\left[\dfrac{(x-x_f)}{L_f}\right]} + \frac{1}{2}\left[z - \alpha \ln\left(\frac{\cosh\dfrac{(h_f - z)}{\alpha}}{\cosh\dfrac{h_f}{\alpha}}\right)\right] \times \frac{\Lambda}{\cosh[(x-x_f)/L_f]} \times \left\{1 - 2\tanh^2\left[\frac{x-x_f}{L_f}\right]\right\}, \quad (8)$$

where $\alpha = 1.2$ km is the depth of the baroclinic zone, $h_f = 3.5$ km is the reference level, and the vertical shear is $\Lambda = 0.003\ s^{-1}$. The main features of this flow, shown in Fig. 14, are that the baroclinicity is confined to the lower layers of the atmosphere ($z \leq h_f$) and that at the surface relatively weak ($\gamma = 0.6$ for $x \geq x_f$), warm southerly flow, and relatively strong ($\gamma = 1.4$ for $x < x_f$), cold

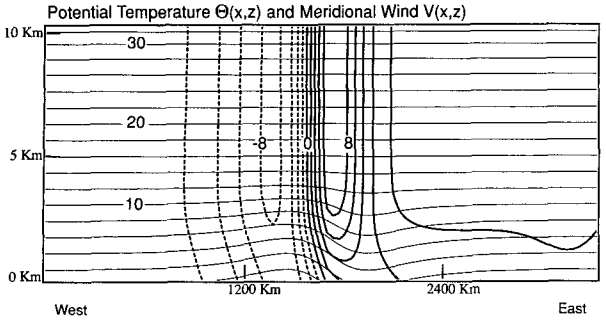

FIG. 14. As in Fig. 11 except for the baroclinic simulations.

northerly flow simulate the frontal circulation shown in Fig. 11.

Significant modifications to the barotropic solution are introduced with surface temperature variations and the associated vertical shear in the frontal circulation, as shown in Fig. 15. The basic characteristics of westward advection on the south of the ridge and eastward advection on the north are the same as those displayed in Fig. 13. However, significant asymmetry appears between the local advection of the warm air to the west and the cold air to the east by the induced mountain anticyclone. In particular, the westward flow to the south of the ridge is much more intense than the eastward flow on the north. Advecting warm air westward produces a hydrostatic pressure fall that intensifies the strong pressure gradients between the developing cyclone to the south and the mountain anticyclone. This pressure gradient enhances the induced westward component of geostrophic flow and further exacerbates the warm advection and cyclonic development. In contrast, eastward cold advection to the north of the ridge creates a hydrostatic pressure rise that weakens the pressure gradients and effectively broadens the mountain anticyclone to the north of the ridge. This effect produces the characteristic dipole seen in observations of orographic cyclogenesis (Fig. 1). If there is an ample supply of warm air to the south or cold air to the north, the pressure will continue to fall and produce a major cyclonic response south of the topography. This response is also found in flows with uniform interior potential vorticity and potential temperature anomalies at the ground. In this case, the flow maximum in the undisturbed front at the surface will be between the warm and cold anomalies and will decay exponentially with height, but the basic pattern of warm advection and associated pressure falls south of the ridge would be similar to that shown in Fig. 15. A quasigeostrophic model should also capture this signature, although the low will tend to be weaker and broader.

The sensitivity of this response to the relative position of the front and the orographic ridge has been examined by placing the front over various sections of the ridge to simulate the frontal progression over topography that occurs in the control solution shown in Fig. 3. At each position, a distinct cyclone formed to the south of the ridge (not shown), so the mechanism of cyclonic vorticity production discussed above operates throughout the period that the front interacts with the orography. If the whole eastward propagating baroclinic system is considered—that is, the parent cyclone and front as in the control solution—it is expected from our previous discussion that the enhanced westward flow south of the ridge due to the modified frontal circulation will delay the eastward progression of the newly generated orographic cyclone and extend the period of cyclogenesis. Further, the parent cyclone on the north will be advected faster to the east by the induced mountain anticyclone.

It is important to note that the circulations produced by this finite-amplitude mechanism represent essentially a transient evolution from the initial condition and are not necessarily evidence of an instability. For example, the flow depicted in Fig. 14 might be unstable according to the mechanisms discussed by Schär and Davies (1990), although that possibility has not been rigorously examined here. However, the flow appears to be stable everywhere away from the mountain, and the response is quite localized, as shown in Fig. 15, which most likely eliminates the mechanism of Schär and Davies (1990) as a generator of the cyclone.

The cyclonic circulation shown in Fig. 15 is quite deep, extending all the way to the rigid lid. This compares well with the cyclonic vorticity distribution in the control solution shown in Fig. 4d. Further, the growth of the disturbance is relatively rapid. The largest surface pressure falls of about 1 hPa/6 h occur during the first 12–24 hours, after which the solution achieves a quasi-steady state. The maximum pressure falls are directly related to the temperature of the warm air that is advected into the cyclone. A stronger temperature gradient will clearly provide more warm air and stronger pressure minima in these simulations. In the control simulation, this temperature gradient is essentially determined by the meridional basic-state temperature gradient (2) and the frontogenesis that takes place during the nonlinear development of the baroclinic wave upstream of the ridge.

It should be pointed out that the cyclone intensification mechanism discussed here is fundamentally different from that of Smith (1984). In Smith's model, the mountain perturbs the basic baroclinic flow in a way that produces a neutral baroclinic wave train in the lee of the ridge. Substantial growth near the ridge requires zero phase velocity, provided in Smith's case by a cross-ridge wind reversal in the vertical. However, this cross-ridge wind reversal is negligible in the control solution shown in Fig. 11 and the basic state shown in Fig. 14. In these cases, there is a cross-ridge wind reversal mainly in the *horizontal,* but it is unclear whether

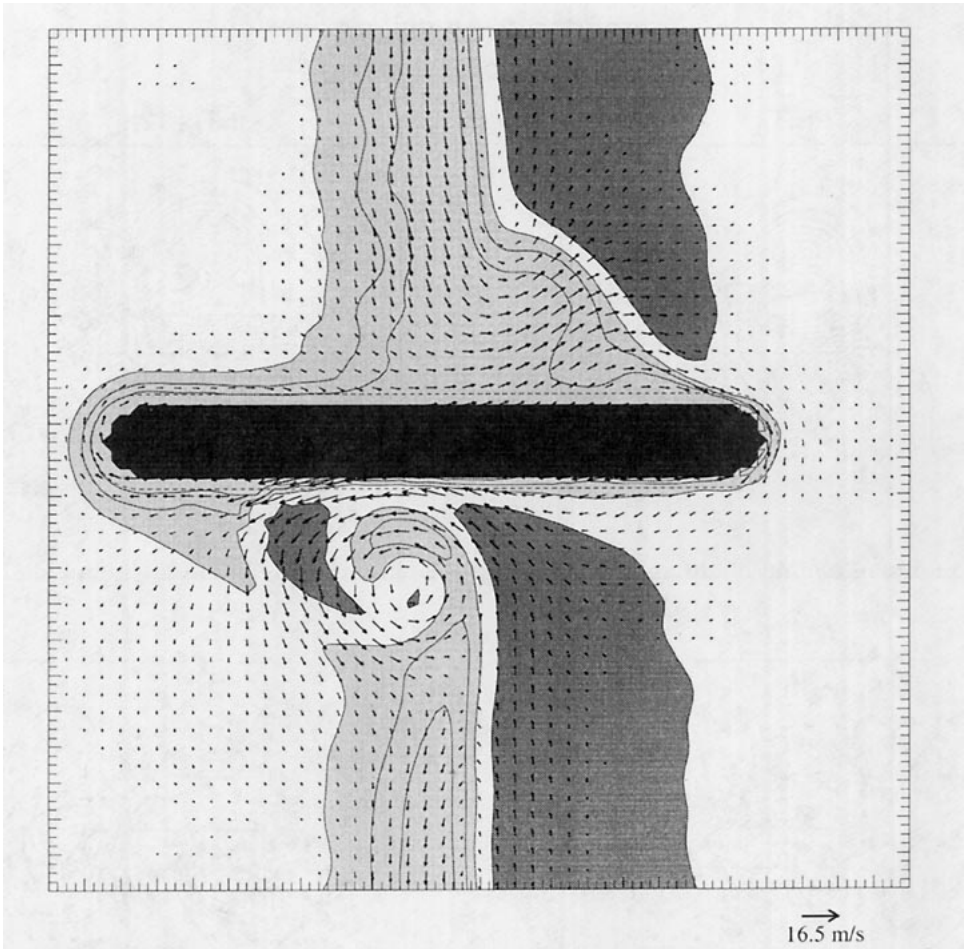

FIG. 15. Potential temperature and horizontal velocity at $z = 1000$ m for the baroclinic simulations. The temperature bands correspond to $\theta < 3$ K (light gray), $3 \text{ K} \leq \theta < 4$ K (white), and $\theta \geq 4$ K (dark gray). The topographic cross section at this height is shaded black. The longest vector corresponds to a speed of 16.5 m s^{-1}. Tick marks are placed every 60 km.

this will support stationary baroclinic waves. Further, only an isolated disturbance on the slope windward of the warm flow (in the lee of the cold flow) is produced, which is not predicted by Smith's theory. The growing pressure gradient between this isolated cyclone and the mountain anticyclone enhances warm advection into the cyclone, which represents the fundamental feedback mechanism responsible for the growth of the disturbance.

To confirm that the mechanism illustrated above operates in the control solutions, the difference between the control solution and a similar solution without topography is shown in Fig. 16. The anomalies in the pressure (upper graphs), the temperature and velocity (middle graphs), and the relative vorticity (lower graphs) are shown for times T_0 and $T_0 + 12$ h at the surface. Attention should be focused on the anomalies to the left of the topography since on the right large perturbations downstream of the topography have already developed. At $t = T_0$ the surface frontal system is responding to the influence of the mountain. We can identify the warm temperature anomaly with westward flow near the ridge (middle graph), similar to the warm circulation of Fig. 15. A low pressure anomaly and cyclonic vorticity associated with that warm pool are found. The circulation intensifies 12 hours later as seen on the panels on the right of Fig. 16. Clearly, the local effect that enhances the baroclinic development has already taken place.

An indirect proof that this finite-amplitude local effect is of major importance in the orographic modification of cyclone development is provided by the fact that the large response observed in the control solution could not be reproduced with numerical solutions in which the mountain ridge was displaced upstream or downstream. In the solutions with the ridge displaced upstream (closer to the left boundary of the channel) the baroclinic eddies reaching the topographic feature

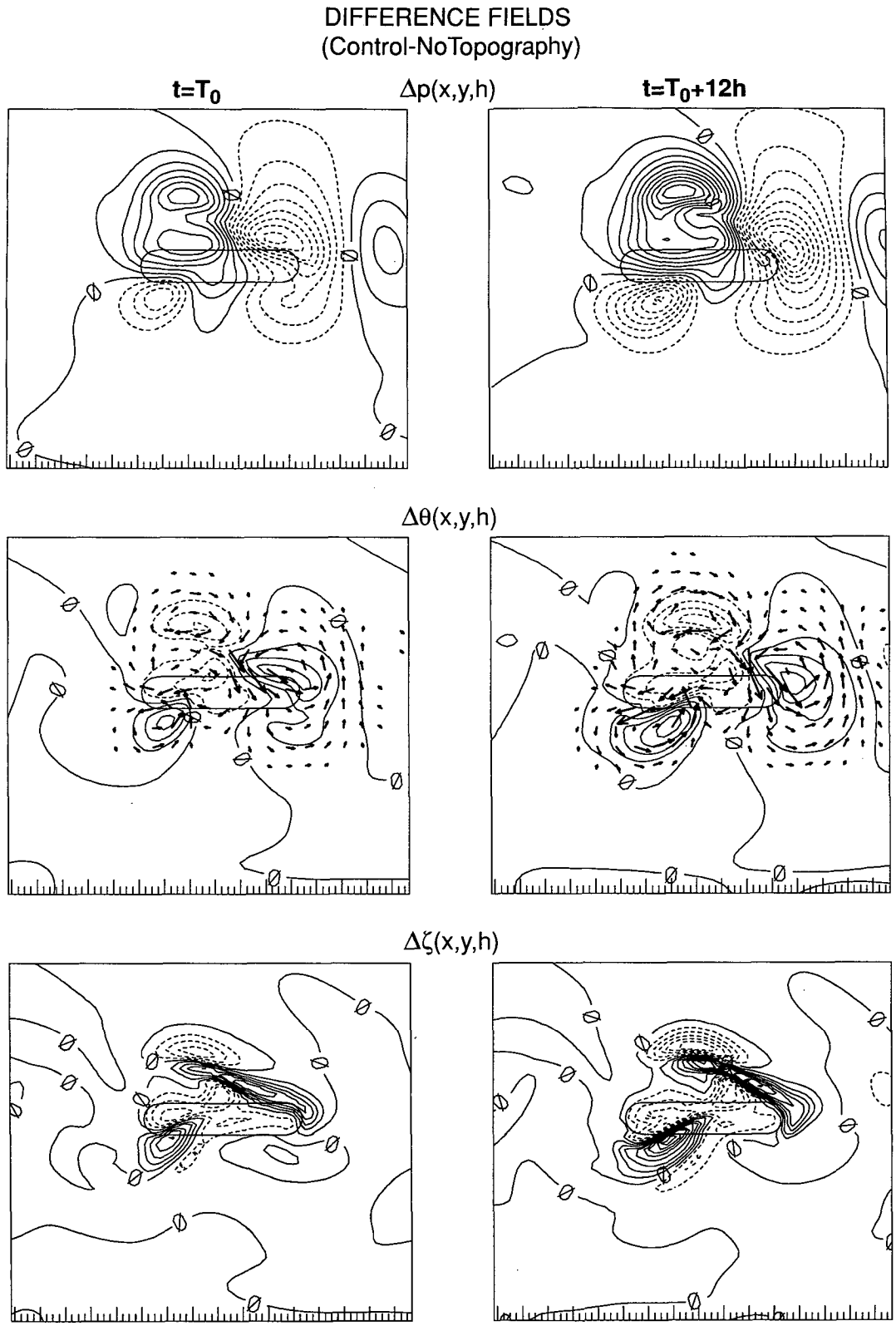

FIG. 16. The anomalies in pressure (top, contours every 1 hPa), temperature and velocity [middle, contours every 2 K and maximum speeds of 18 m s^{-1} ($t = T_0$) and 25 m s^{-1} ($t = T_0 + 12$ h)], and relative vorticity (bottom, contour every 2×10^{-5} s^{-1}) at $t = T_0$ (left panels) and $t = T_0 + 12$ h (right panels) in the control simulation at the surface. Tick marks along the bottom borders are placed every 100 km.

DEVELOPMENT OF AN OROGRAPHIC CYCLONE

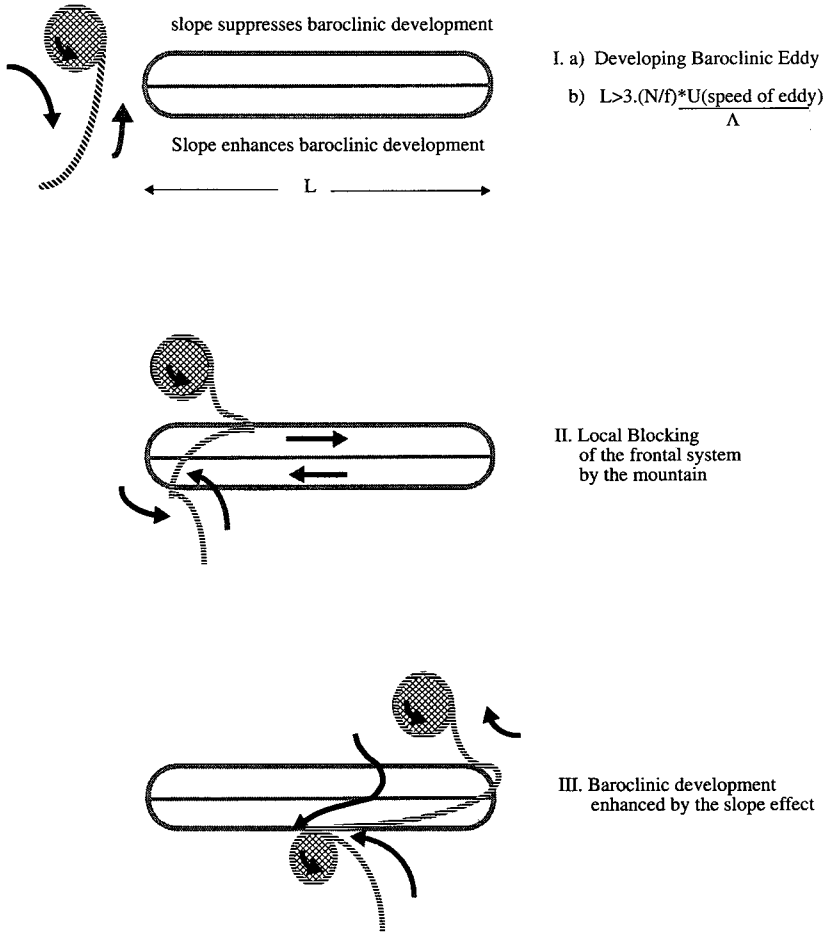

FIG. 17. A schematic diagram of orographic cyclogenesis near an isolated mountain ridge.

were small, as they did not have time to grow to a finite amplitude. The associated meridional circulation in the frontal system that impinged on the topography was too weak to interact with the mountain and produce significant cyclogenesis by this process. Moving the ridge farther downstream also failed to produce significant orographic enhancement, because in that case the baroclinic eddies reaching the topography were already in the decay stage, with mostly occluded fronts and relatively weak surface temperature contrasts.

5. Conclusions

The orographic modification of cyclone development has been examined with primitive equation simulations of the interaction between a baroclinic wave and a mountain ridge. Many of the features observed in cases of orographic cyclogenesis are reproduced in these simulations. A summary of the development process is provided in Fig. 17. A relatively intense cyclone forms on the south side of the orographic ridge, distinct from the parent cyclone that remains along the axis of the jet north of the ridge. Inspection of both the control and elongated ridge solutions establishes that this development is characteristic of convective rather than absolute instability. The measured growth of the intensity of the orographic vortex center is larger than the baroclinic eddies that grow unmodified by orography. Both wave-scale and local-scale mechanisms are evaluated to determine their respective roles in orographic cyclogenesis.

A series of integrations that examine the growth of small and finite-amplitude normal modes reveals the sensitivity of the structure and growth rate of these waves to the characteristics of the topography. It is found that baroclinic development is enhanced where

the topography slopes in the same direction as the isentropes, in agreement with previous analyses. This condition is met on the south side of the ridge (Fig. 17a) in the simulations presented here. However, it is also found that since eddies should remain on the south flank of the ridge to experience this enhanced growth, orographic cyclogenesis at mountain ranges with lengths comparable to the Alps requires surface easterly winds. It is unlikely that this condition will be realized in most cases of Alpine cyclogenesis, and in particular, neither the 3–5 March case nor the control simulation satisfied this criterion. Therefore, the enhancement of wave-scale development on the south slope of the ridge is by itself insufficient to account for orographic cyclogenesis. It is suggested that zonally localized processes in the interaction between the baroclinic eddy and the mountain are paramount for realistic enhancement of the cyclogenesis.

The local modification of the circulation in the mature front associated with the baroclinic cyclone impinging on the topographic ridge seems to be responsible for the orographic cyclogenesis. It has been shown that the warm southerly flow in the front is diverted westward by the mountain ridge (Fig. 17b). This warm advection produces a pressure fall that intensifies the strong pressure gradient between the mountain anticyclone and the developing cyclone to the south. This process enhances the induced westward geostrophic flow and further exacerbates the warm advection and resultant cyclonic circulation south of the ridge (Figs. 17b,c). In contrast, cold northerly flow is diverted eastward as it approaches the mountain, producing a pressure rise that effectively broadens the mountain anticyclone to the north of the ridge. This effect combines with the developing low south of the ridge to produce the characteristic pressure dipole observed in orographic cyclogenesis. Although this mechanism does not require the conditions on the mean flow noted above, a mature front with a considerable temperature contrast and strong circulation is needed for an intense response. In contrast, orographic cyclogenesis may be weak or nonexistent in cases where the front is just forming or is in the occluded stage when the temperature contrasts in the front are relatively small.

Other mechanisms may even further enhance cyclogenesis south of an isolated ridge. For example, a heat source south of the mountain ridge may increase the baroclinicity there and favor development on the south slope. In cases of Alpine cyclogenesis, such a heat source may be represented by the Mediterranean Sea. Numerical simulations similar to the control experiment discussed in section 2, except with a stationary heat source south of the ridge, have confirmed this point, although they are not discussed here. This mechanism and other factors that include surface friction and the diabatic effects of moisture represent the focus of future research.

Acknowledgments. The authors gratefully acknowledge Noboru Nakamura for providing the initial version of the model, and Edmund Chang for aid in the subsequent code modifications. Steven Garner provided the Poisson solver that was used during the early development of the ZETA model. We would also like to thank Edmund Chang, Steven Garner, Antonio Speranza, and two anonymous reviewers for their comments on the manuscript.

APPENDIX

The ZETA Model

The numerical primitive equation model used in the simulations presented here is similar in concept to the anelastic hydrostatic model used by Ross and Orlanski (1982). A new vertical terrain-following coordinate is introduced, given by

$$Z = e^{-\epsilon[(z-h(x,y))/(H-h(x,y))]}, \qquad \text{(A1)}$$

where z is physical height, $h(x, y)$ represents the height profile of the isolated mountain, and H is the height of the model rigid lid. Larger values of ϵ place more model levels and higher resolution near the ground. An additional advantage of employing such a physically based vertical coordinate is its ease of use in more applied meteorological research applications, such as four-dimensional data assimilation. In this case, a physical vertical coordinate is more compatible with the newer atmospheric observing systems currently being deployed, such as Doppler radar and wind profilers that, in contrast to, say, rawindsondes, are not based on a pressure coordinate.

a. *Governing equations*

The anelastic form of the continuity equation expressed in the vertical coordinate (A1) is given by

$$\nabla\cdot(\rho_0\delta_Z\mathbf{v}) + \frac{\partial}{\partial Z}(\rho_0\delta_Z\dot{Z}) = 0, \qquad \text{(A2)}$$

where in the present case ρ_0 is at most a function of z. In this model, the horizontal momentum equation in flux vector form is expressed as

$$\frac{\partial}{\partial t}(\rho_0\delta_Z\mathbf{v}) + \nabla\cdot(\rho_0\delta_Z\mathbf{v}\mathbf{v}) + \frac{\partial}{\partial Z}(\rho_0\delta_Z\dot{Z}\mathbf{v}) + f\mathbf{k}\times\rho_0\delta_Z\mathbf{v} = -c_p\Theta_0\rho_0\delta_Z\nabla\pi + \frac{g\theta}{\Theta_0}\rho_0\delta_Z\nabla z + \mu\rho_0\delta_Z\nabla^2\mathbf{v}. \qquad \text{(A3)}$$

In (A3), Θ_0 is a constant reference potential temperature set to 302 K, θ is the deviation from Θ_0, $\mathbf{v}$ is the horizontal velocity, and π is a nondimensional function of pressure given by $\pi = (p/p_0)^\kappa$. The last term in (A3) represents weak diffusion along constant Z surfaces. The value $\mu = 10^5\,(\Delta x/100\text{ km})^2\text{ m}^2\text{ s}^{-1}$ was used in

the simulations presented above, where Δx is the grid resolution in kilometers. According to (A1), the physical height z and the geometric conversion factor δ_Z are given by

$$z = h(x, y) - \frac{(H - h(x, y))}{\epsilon} \ln(Z), \quad \text{(A4)}$$

$$\delta_Z \equiv \frac{\partial z}{\partial Z} = -\frac{(H - h(x, y))}{\epsilon Z}. \quad \text{(A5)}$$

The hydrostatic equation in this vertical coordinate is

$$c_p \Theta_0 \frac{\partial \pi}{\partial Z} = \delta_Z \frac{g\theta}{\Theta_0}, \quad \text{(A6)}$$

and the evolution of the potential temperature θ is governed by

$$\frac{\partial}{\partial t}(\rho_0 \delta_Z \theta) + \nabla \cdot (\rho_0 \delta_Z \theta \mathbf{v}) + \frac{\partial}{\partial Z}(\rho_0 \delta_Z \theta \dot{Z}) = \mu \rho_0 \delta_Z \nabla^2 \theta. \quad \text{(A7)}$$

At present, the model is bounded by impermeable rigid walls in the meridional direction. Zonal periodicity is enforced; however, sponge layers may be included at the east and west boundaries in order to 1) force the model with arbitrary conditions at these boundaries, if desired, and 2) prevent disturbances generated in the course of model integration from reappearing once they have exited the domain. In the simulations presented above, for example, the baroclinic waves generated downstream of the ridge (Fig. 3) do not reappear at the upstream (western) boundary. The model variables are damped toward the prescribed boundary values by specifying linear combinations of the model variables and prescribed values within the sponge layers, which are typically ten grid points wide.

The topography at the lower boundary ($Z = 1$) and the rigid upper lid ($Z = e^{-\epsilon}$) are material surfaces so that $\dot{Z}$ vanishes at these levels. As a consequence of these boundary conditions, the integrated horizontal divergence over the depth of the atmosphere vanishes. This may be seen by integrating (A2) through the entire vertical column and applying the boundary conditions $\dot{Z} = 0$ at the upper and lower boundaries:

$$\nabla \cdot \int_1^{e^{-\epsilon}} (\rho_0 \delta_Z \mathbf{v}) dZ = 0. \quad \text{(A8)}$$

It is then useful to consider the barotropic and baroclinic flows separately. To this end, the pressure variable π may be partitioned into $\pi(x, y, Z) = \pi_L(x, y) + \pi_h(x, y, Z)$ (Ross and Orlanski 1982), where π_L is the pressure at the rigid lid and π_h is the hydrostatic pressure defined by (A6) as

$$\pi_h(x, y, Z) = \frac{g c_p}{\Theta_0^2} \int_Z^{e^{-\epsilon}} (\delta_Z \theta) dZ', \quad \text{(A9)}$$

which is zero at the rigid lid. The horizontal momentum equation (A3) may then be written as

$$\frac{\partial}{\partial t}(\rho_0 \delta_Z \mathbf{v}) = \mathbf{G} - c_p \Theta_0 \rho_0 \delta_Z \nabla \pi_L, \quad \text{(A10)}$$

where $\mathbf{G} = (G_u, G_v)$ represents the momentum tendencies associated with advection, the Coriolis force, hydrostatic pressure gradients, and dissipation.

According to (A8), a streamfunction may be introduced that satisfies

$$\int_1^{e^{-\epsilon}} (\rho_0 \delta_Z \mathbf{v}) dZ = -\mathbf{k} \times \nabla \Psi. \quad \text{(A11)}$$

Then the vertical integral of (A10) may be written as

$$\frac{\partial}{\partial t}(-\mathbf{k} \times \nabla \Psi) = \int_1^{e^{-\epsilon}} \mathbf{G} dZ - M c_p \Theta_0 \nabla \pi_L, \quad \text{(A12)}$$

where

$$M = \int_1^{e^{-\epsilon}} \rho_0 \delta_Z dZ \quad \text{(A13)}$$

is the mass per unit area in the vertical column. Equations for the streamfunction Ψ and pressure π_L may be derived from (A12) and are given, respectively, by

$$\frac{\partial}{\partial t}\left(\nabla \cdot \frac{1}{M} \nabla \Psi\right) = -\nabla \times \frac{1}{M} \int_1^{e^{-\epsilon}} \mathbf{G} dZ \quad \text{(A14)}$$

and

$$\nabla \cdot M \nabla \pi_L = \frac{1}{c_p \Theta_0} \nabla \cdot \int_1^{e^{-\epsilon}} \mathbf{G} dZ. \quad \text{(A15)}$$

Clearly, Ψ is constant along the north and south boundaries, and the components of (A12) may be used to calculate π_L along these boundaries and the western boundary. Of course, both variables are periodic in the zonal direction.

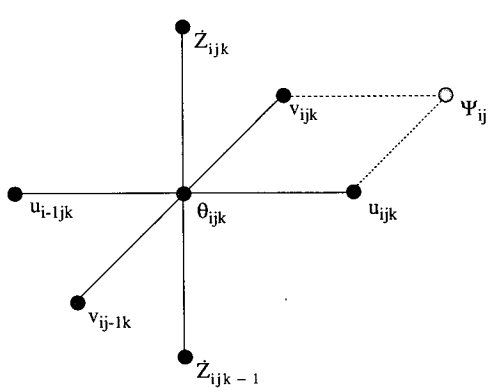

FIG. 18. The distribution of variables in the ZETA model. Although the barotropic streamfunction Ψ is independent of Z, its relative horizontal position is shown here for convenience.

An expression for the rigid-lid pressure π_L may be derived from (A12) and substituted into (A10) to provide an alternate form of the momentum equation

$$\frac{\partial}{\partial t}(\rho_0\delta_Z\mathbf{v}) = \mathbf{G} - \frac{\rho_0\delta_Z}{M}\left[\int_1^{e-\epsilon}\mathbf{G}dZ - \frac{\partial}{\partial t}(-\mathbf{k}\times\nabla\Psi)\right]. \quad \text{(A16)}$$

The first two terms in (A16) represent the baroclinic tendencies, and the last term represents the barotropic tendencies that are required to ensure that the boundary conditions on the top and bottom boundaries ($\dot{Z} = 0$) are satisfied. Either (A10) or (A16) may be used to integrate the horizontal momentum in time, but we have adopted (A16) for use in the numerical calculations presented above.

b. Discrete equations

Centered differences in time and second-order spatial finite differences on an Arakawa C grid (Mesinger and Arakawa 1976) are used in the discretization of the governing equations (A2), (A6), (A7), and (A14)–(A16). The C grid possesses superior characteristics in calculating the divergence and, as a consequence, is perhaps the best grid to simulate gravity waves and convective processes. This is a primary consideration in applying this model to mesoscale problems. The relative distribution of variables is shown in Fig. 18. Variables that are not explicitly shown in Fig. 18 are defined at potential temperature points. There are IX points in the zonal direction, where periodicity yields $q_{1jk} = q_{IXjk}$ for any variable q; IY points in the meridional direction, where v_{i2k} and v_{iIY-1k} both vanish at the walls; and IZ points in the vertical, where $\dot{Z}_{ij1} = 0$ along the topography and $\dot{Z}_{ijIZ-1} = 0$ at the rigid upper lid. In fact, one reason for using (A16) rather than (A10) is that the boundary streamfunction is defined exactly at the meridional walls (Fig. 18), while the rigid-lid pressure is not, so that an accurate and consistent application of the boundary conditions ($v = 0$, Ψ = constant at the walls) is possible. A weak Robert filter (Asselin 1972) is applied every time step to damp the computational mode that arises in the leapfrog time scheme. The following operators provide a notational aid in discussing the discretized form of the governing equations:

$$\bar{q}^x = \frac{1}{2}(q_{i+1jk} + q_{ijk}), \quad \text{(A17)}$$

$$\Delta_x q = \frac{1}{\Delta x}(q_{ijk} - q_{i-1jk}). \quad \text{(A18)}$$

These operators may be applied to any variable q. Similar averaging and differencing operators may be derived for the other independent variables.

The discrete form of the hydrostatic and continuity equations provide diagnostic expressions for the hydrostatic pressure π_h and the vertical velocity $\dot{Z}$ at time step n:

$$(\pi_h^n)_{ijk-1} = (\pi_h^n)_{ijk} + \Delta Z\frac{g}{c_p\Theta_0^2}\overline{(\delta_Z\theta^n)}^Z, \quad \text{(A19)}$$

$$(\overline{\rho_0\delta_Z}^Z\dot{Z}^n)_{ijk-1} = (\overline{\rho_0\delta_Z}^Z\dot{Z}^n)_{ijk} - \Delta Z[\Delta_x(\rho_0\bar{\delta}_Z^x u^n) + \Delta_y(\rho_0\bar{\delta}_Z^y v^n)]. \quad \text{(A20)}$$

The tendencies in the momentum and thermodynamic equations are discretized in a manner similar to that of Williams (1969) and are given by

$$G_u = -\left[\Delta_x\left(\rho_0\overline{\delta_Z}^x u^n\,\overline{u^n}^x\right) + \Delta_y\left(\rho_0\overline{\delta_Z}^y v^n\,\overline{u^n}^y\right) + \Delta_Z\left(\overline{\rho_0\delta_Z}^Z\dot{Z}^n\,\overline{u^n}^Z\right)\right] + \rho_0\overline{\delta_Z}^x\left(-c_p\Theta_0\Delta_x\pi_h^n + \frac{g}{\Theta_0}\overline{\theta^n}^x\Delta_x z + f\overline{v^n}^{xy} + \mu(\Delta_x\Delta_x u^{n-1} + \Delta_y\Delta_y u^{n-1})\right), \quad \text{(A21)}$$

$$G_v = -\left[\Delta_x\left(\rho_0\overline{\delta_Z}^x u^n\,\overline{v^n}^x\right) + \Delta_y\left(\rho_0\overline{\delta_Z}^y v^n\,\overline{v^n}^y\right) + \Delta_Z\left(\overline{\rho_0\delta_Z}^Z\dot{Z}^n\,\overline{v^n}^Z\right)\right] + \rho_0\overline{\delta_Z}^y\left(-c_p\Theta_0\Delta_y\pi_h^n + \frac{g}{\Theta_0}\overline{\theta^n}^y\Delta_y z - f\overline{u^n}^{xy} + \mu(\Delta_x\Delta_x v^{n-1} + \Delta_y\Delta_y v^{n-1})\right), \quad \text{(A22)}$$

$$G_\theta = -[\Delta_x(\rho_0\overline{\delta_Z}^x u^n\overline{\theta^n}^x) + \Delta_y(\rho_0\overline{\delta_Z}^y v^n\overline{\theta^n}^y) + \Delta_Z(\overline{\rho_0\delta_Z}^Z\dot{Z}^n\overline{\theta^n}^Z)] + \rho_0\delta_Z\mu(\Delta_x\Delta_x\theta^{n-1} + \Delta_y\Delta_y\theta^{n-1}). \quad \text{(A23)}$$

Note that the dissipation in (A21)–(A23) is applied at time step $n-1$ for numerical stability. By defining

$$u_H = u^{n-1} + 2\Delta t G_u/\rho_0\overline{\delta_Z}^x, \quad \text{(A24)}$$

$$v_H = v^{n-1} + 2\Delta t G_v/\rho_0\overline{\delta_Z}^y, \quad \text{(A25)}$$

and using the streamfunction definition (A11), the discretized components of the momentum equation (A16) may be written as

$$u^{n+1} = u^{n-1} - \frac{\Delta Z}{M}\sum_{k=2}^{IZ-1}\rho_0\overline{\delta_Z}^x u_H + \frac{1}{M}\Delta_y\Psi^{n+1}, \quad \text{(A26)}$$

$$v^{n+1} = v^{n-1} - \frac{\Delta Z}{M} \sum_{k=2}^{IZ-1} \rho_0 \overline{\delta_Z}^{y} v_H - \frac{1}{M} \Delta_x \Psi^{n+1}, \quad \text{(A27)}$$

and the thermodynamic equation as

$$\theta^{n+1} = \theta^{n-1} + 2\Delta t G_\theta / \rho_0 \delta_Z. \quad \text{(A28)}$$

The streamfunction Ψ^{n+1} is found from the time discretization of (A14):

$$\Delta_x\left(\frac{1}{M}\Delta_x\Psi^{n+1}\right) + \Delta_y\left(\frac{1}{M}\Delta_y\Psi^{n+1}\right) = \Delta_y\left(\frac{\Delta Z}{M}\sum_{k=2}^{IZ-1}\rho_0\overline{\delta_Z}^{x} u_H\right) - \Delta_x\left(\frac{\Delta Z}{M}\sum_{k=2}^{IZ-1}\rho_0\overline{\delta_Z}^{y} v_H\right). \quad \text{(A29)}$$

The equations (A19), (A20), and (A26)–(A29) are solved for the model variables π_h, $\dot{Z}$, $\mathbf{v}$, θ, and Ψ, respectively, at each time step. The pressure at the lid π_L is calculated from (A15) only when the model variables are saved to a history, and the complete pressure π is required. The solutions to the self-adjoint elliptic equations (A15) and (A29) are obtained with a multigrid method from the package MUDPACK (Adams et al. 1992).

REFERENCES

Adams, J., R. Garcia, B. Gross, J. Hack, D. Haidvogel, and V. Pizzo, 1992: Applications of multi-grid software in the atmospheric sciences. *Mon. Wea. Rev.*, **120,** 1447–1458.

Asselin, R., 1972: Frequency filter for time integrations. *Mon. Wea. Rev.*, **100,** 487–490.

Bleck, R., and C. Mattocks, 1984: A preliminary analysis of the role of potential vorticity in Alpine lee cyclogenesis. *Contrib. Atmos. Phys.*, **62,** 30–45.

Blumsack, S. L., and P. J. Gierasch, 1972: Mars: The effects of topography on baroclinic instability. *J. Atmos. Sci.*, **29,** 1081–1089.

Buzzi, A., and A. Speranza, 1986: A theory of deep cyclogenesis in the lee of the Alps. Part II: Effects of finite topographic slope and height. *J. Atmos. Sci.*, **43,** 2826–2837.

——, and E. Tosi, 1989: Statistical behavior of transient eddies near mountains and implications for theories of lee cyclogenesis. *J. Atmos. Sci.*, **46,** 1233–1249.

Egger, J., 1988: Aline lee cyclogenesis: Verification of theories. *J. Atmos. Sci.*, **45,** 2187–2203.

Malguzzi, P., A. Trevisan, and A. Speranza, 1987: Effects of finite height topography on nongeostrophic baroclinic instability: Implications to theories of lee cyclogenesis. *J. Atmos. Sci.*, **44,** 1475–1482.

Mechoso, C. R., 1980: Baroclinic instability of flows along sloping boundaries. *J. Atmos. Sci.*, **37,** 1393–1399.

Merkine, L. O., 1977: Convective and absolute instability of baroclinic eddies. *Geophys. Astrophys. Fluid Dyn.*, **9,** 129–157.

Mesinger, F., and A. Arakawa, 1976: Numerical methods used in atmospheric models. Vol. 1. GARP Publ. Ser. No. 17, WMO, 64 pp.

——, R. Pierrehumbert, 1986: Alpine lee cyclogenesis: Numerical simulation and theory. Scientific Results of the Alpine Experiment, Vol. 1. GARP Publ. Ser. 27, 141–165.

Orlanski, I., 1969: The influence of bottom topography on the stability of jets in a baroclinic fluid. *J. Atmos. Sci.*, **26,** 1216–1232.

——, and M. D. Cox, 1973: Baroclinic instability in ocean currents. *Geophys. Fluid Dyn.*, **4,** 297–332.

Pedlosky, J., 1987: *Geophysical Fluid Dynamics.* 2d ed. Springer-Verlag, 710 pp.

Pierrehumbert, R., 1984: Local and global baroclinic instability of zonally varying flow. *J. Atmos. Sci.*, **41,** 2141–2162.

——, 1985: A theoretical model of orographically modified cyclogenesis. *J. Atmos. Sci.*, **42,** 1244–1258.

——, 1986: Spatially amplifying modes of the Charney baroclinic-instability problem. *J. Fluid Mech.*, **170,** 293–317.

Ross, B. B., and I. Orlanski, 1982: The evolution of an observed cold front. Part I: Numerical simulation. *J. Atmos. Sci.*, **39,** 296–327.

Schär, C., 1990: Quasi-geostrophic lee cyclogenesis. *J. Atmos. Sci.*, **47,** 3044–3066.

——, and H. C. Davies, 1990: An instability of mature cold fronts. *J. Atmos. Sci.*, **47,** 929–950.

Smith, R. B., 1984: A theory of lee cyclogenesis. *J. Atmos. Sci.*, **41,** 1159–1168.

——, 1986: Further development of a theory of lee cyclogenesis. *J. Atmos. Sci.*, **43,** 1582–1602.

Speranza, A., A. Buzzi, A. Trevisan, and P. Malguzzi, 1985: A theory of deep cyclogenesis in the lee of the Alps. Part I: Modifications of baroclinic instability by localized topography. *J. Atmos. Sci.*, **42,** 1521–1535.

Tafferner, A., and J. Egger: 1990: Test of theories of lee cyclogenesis: ALPEX cases. *J. Atmos. Sci.*, **47,** 2417–2428.

Tibaldi, S., A. Buzzi, and A. Speranza, 1990: Orographic cyclogenesis. *Extratropical Cyclones, The Erik Palmén Memorial Volume,* C. Newton and E. O. Holopainen, Eds., Amer. Meteor. Soc., 107–127.

Trevisan, A., and U. Giostra, 1990: Dynamical criteria determining lee cyclogenesis. *J. Atmos. Sci.*, **47,** 2400–2408.

Williams, G. P., 1969: Numerical integrations of the three-dimensional Navier-Stokes equations for incompressible flow. *J. Fluid Mech.*, **37,** 727–750.